THE PLANT CELL

Imaging of plant calcium-sensor kinase conformation monitors real time calcium-dependent decoding *in planta*

Anja Liese [1,2] Bernadette Eichstädt [2] Sarah Lederer [1] Philipp Schulz [2] Jan Oehlschläger [1] Susanne Matschi [1] José A Feijó [3] Waltraud X. Schulze [4] Kai R. Konrad [5] and Tina Romeis [1,2,*]

1 Department for Biochemistry of Plant Interactions, Leibniz Institute of Plant Biochemistry, D-06120 Halle (Saale), Germany
2 Dahlem Centre of Plant Sciences, Freie Universität Berlin, D-14195 Berlin, Germany
3 Department of Cell Biology & Molecular Genetics, University of Maryland, 2136 Bioscience Research Bldg, College Park, MD 20742-5815, USA
4 Plant Systems Biology, Universität Hohenheim, D-70593 Stuttgart, Germany
5 Julius-Von-Sachs Institute for Biosciences, Julius Maximilians Universität Würzburg, D-97082 Würzburg, Germany

*Author for correspondence: Tina.Romeis@ipb-halle.de
The authors responsible for distribution of materials integral to the findings presented in this article in accordance with the policy described in the Instructions for Authors (https://academic.oup.com/plcell/) are: Tina Romeis (Tina.Romeis@ipb-halle.de) and Anja Liese (Anja.Liese@ipb-halle.de).

Abstract

Changes in cytosolic calcium (Ca^{2+}) concentration are among the earliest reactions to a multitude of stress cues. While a plethora of Ca^{2+}-permeable channels may generate distinct Ca^{2+} signatures and contribute to response specificities, the mechanisms by which Ca^{2+} signatures are decoded are poorly understood. Here, we developed a genetically encoded Förster resonance energy transfer (FRET)-based reporter that visualizes the conformational changes in Ca^{2+}-dependent protein kinases (CDPKs/CPKs). We focused on two CDPKs with distinct Ca^{2+}-sensitivities, highly Ca^{2+}-sensitive Arabidopsis (*Arabidopsis thaliana*) *At*CPK21 and rather Ca^{2+}-insensitive *At*CPK23, to report conformational changes accompanying kinase activation. In tobacco (*Nicotiana tabacum*) pollen tubes, which naturally display coordinated spatial and temporal Ca^{2+} fluctuations, CPK21-FRET, but not CPK23-FRET, reported oscillatory emission ratio changes mirroring cytosolic Ca^{2+} changes, pointing to the isoform-specific Ca^{2+}-sensitivity and reversibility of the conformational change. In Arabidopsis guard cells, CPK21-FRET-monitored conformational dynamics suggest that CPK21 serves as a decoder of signal-specific Ca^{2+} signatures in response to abscisic acid and the flagellin peptide flg22. Based on these data, CDPK-FRET is a powerful approach for tackling real-time live-cell Ca^{2+} decoding in a multitude of plant developmental and stress responses.

Introduction

Calcium (Ca^{2+}) is the most important second messenger involved in signaling in practically all aspects of eukaryotic stress responses and development. The specificity of Ca^{2+} signaling is determined by the generation of a Ca^{2+}-concentration increase (encoding), followed by Ca^{2+} binding to proteins that convert Ca^{2+} signals into cellular responses (decoding) (Tian et al., 2020). Ca^{2+} signatures are defined based on the magnitude, number, duration, and location of Ca^{2+} transients and are generated by the coordinated actions of Ca^{2+} channels and transporters (Yuan et al., 2014; Toyota et al., 2018; Tian et al., 2019; Thor et al., 2020; Tian et al., 2020; Bjornson et al., 2021; Köster et al., 2022; Xu et al., 2022). With respect to Ca^{2+} encoding, major advances in Ca^{2+} imaging have facilitated the visualization of Ca^{2+} dynamics and Ca^{2+} permeable channel activities in real-time (Thor and Peiter, 2014; Gutermuth et al., 2018; Toyota et al., 2018; Huang et al., 2019; Tian et al., 2019; Mou et al., 2020; Thor et al., 2020; Waadt et al., 2020; Bi et al., 2021; Bjornson et al., 2021; Eichstädt et al., 2021; Li et al., 2021; Guo et al., 2022; Tan et al., 2022; Xu et al., 2022). Yet, the Ca^{2+} decoding step, and in particular monitoring it in real-time in living cells, remains a major challenge.

IN A NUTSHELL

Background: Changes in cytosolic calcium (Ca^{2+}) concentration are among the earliest reactions in signaling in practically all aspects of eukaryotic life. Ca^{2+}-dependent protein kinases (CDPKs) bind Ca^{2+} directly and translate the Ca^{2+}-signal into protein phosphorylation patterns. CDPK-dependent translation of Ca^{2+}-signals includes a conformational change of the protein itself as a requirement for kinase activity. However, elucidating isoform specificity in Ca^{2+} decoding via CDPKs remains a major challenge.

Question: How can we visualize the Ca^{2+}-dependent conformational activation and inactivation of CDPKs?

Findings: We developed a genetically encoded fluorescent biosensor for CDPK conformational activation named CPKaleon. The regulatory Ca^{2+}-binding domain of two *Arabidopsis thaliana* CDPKs (CPK21 and CPK23) was positioned between fluorescent proteins, allowing energy transfer (Förster resonance energy transfer, FRET) between these two fluorescent proteins. FRET measurements reported the Ca^{2+}-dependent conformational change during the CDPK activation process. These fluorescence-based measurements recorded *in vivo* conformational activation and inactivation in tobacco pollen tubes and Arabidopsis guard cells in real time. We observed isoform-specific Ca^{2+}-sensitivity and reversibility of the conformational change both *in vitro* and *in vivo*.

Next steps: We plan to use the CPKaleon approach to study additional CPDK isoforms. This would allow us to record Ca^{2+}-decoding via CDPKs in real time and to uncover the function(s) of CDPKs in signaling pathways of interest.

Ca^{2+}-dependent protein kinases (CDPKs) (CPKs in *Arabidopsis thaliana*) are Ca^{2+} sensor kinases specific to plants and important human parasites (Billker et al., 2009; Yip Delormel and Boudsocq, 2019). CDPKs are able to bind Ca^{2+} directly and to relay the Ca^{2+} signal into protein phosphorylation (Harmon et al., 2000; Liese and Romeis, 2013; Simeunovic et al., 2016; Bender et al., 2018; Kudla et al., 2018; Yip Delormel and Boudsocq, 2019). Ca^{2+}-decoding can be considered a consecutive three reaction process: (i) Ca^{2+} sensing via Ca^{2+} binding to EF-hand motifs, (ii) an induced conformational change (required for CDPK activation), and (iii) its relay (translation) into a response output by targeted protein phosphorylation (CDPK activity). In plants, the CDPK gene family functions in abiotic and biotic stress responses and in developmental signaling (Boudsocq et al., 2010; Geiger et al., 2010; Geiger et al., 2011; Gutermuth et al., 2013; Matschi et al., 2013; Monaghan et al., 2014; Brandt et al., 2015; Liu et al., 2017; Durian et al., 2020; Fu et al., 2022).

CDPKs consist of an N-terminal variable domain, which may harbor myristoylation and palmitoylation membrane-localization motifs, followed by a serine/threonine protein kinase domain, a pseudosubstrate segment (PS) and a calmodulin-like domain (CLD) containing four consensus Ca^{2+}-binding EF-hand motifs (Figure 1A) (Harmon et al., 2000; Liese and Romeis, 2013; Simeunovic et al., 2016; Bender et al., 2018; Kudla et al., 2018). In a CDPK activation model based on the X-ray structure of CDPK1 from the human parasite *Toxoplasma gondii* (Tg), the substrate binding site of the kinase domain is blocked via interaction with the PS in the inactive state (Ojo et al., 2010; Wernimont et al., 2010). In this inactive state, the PS builds a dumbbell shaped domain together with the CLD. Upon Ca^{2+} binding of all four EF-hand motifs, the PS and CLD translocate 135° clockwise on the other side of the kinase domain. The liberated substrate binding site

of the kinase domain can now interact with substrate proteins, which is a requirement for catalyzing ATP-dependent phosphotransfer. In general, biochemical assessment of CDPK activity solely evaluates enzyme activity based on its catalytic transphosphorylation efficiency but does not address the conformational changes in CDPK during the activation process.

We previously investigated two CDPKs from *A. thaliana*, CPK21 and CPK23, which are implicated in plant abiotic stress signaling, where they participate in the abscisic acid (ABA)-mediated control of stomatal aperture. Both enzymes are involved in the ABA-dependent activation of SLOW ANION CHANNEL 1 (SLAC1) and SLAC1 HOMOLOG 3 (SLAH3) to mediate stomatal closure (Geiger et al., 2010; Geiger et al., 2011; Scherzer et al., 2012; Brandt et al., 2015). During this process, the Ca^{2+}-dependent activation of SLAC1-type anion channels was predominantly assigned to CPK21 because CPK23 displayed a rather Ca^{2+} insensitive activity (Geiger et al., 2010; Scherzer et al., 2012). Remarkably, the same anion channels are also associated with stomatal closure in response to the flagellin peptide flg22, a pathogen-associated molecular pattern signal, as part of the plant pre-invasive immunity program that prevents further pathogen invasion through open stoma (Guzel Deger et al., 2015; Wang and Gou, 2021). The dependence of flg22-induced stomatal closure on Ca^{2+} signaling, combined with the activation of SLAC1 type anion channels as downstream recipients of Ca^{2+} signaling, points toward a role for CDPKs as prospective Ca^{2+} decoders (Thor and Peiter, 2014; Guzel Deger et al., 2015; Keinath et al., 2015; Thor et al., 2020).

Here, we developed a CDPK-associated ratiometric Förster resonance energy transfer (FRET) chimera that reports the Ca^{2+}-dependent conformational change during the CDPK activation process. We called this sensor CPKaleon containing CPK in the name and aleon is a resemblance to other
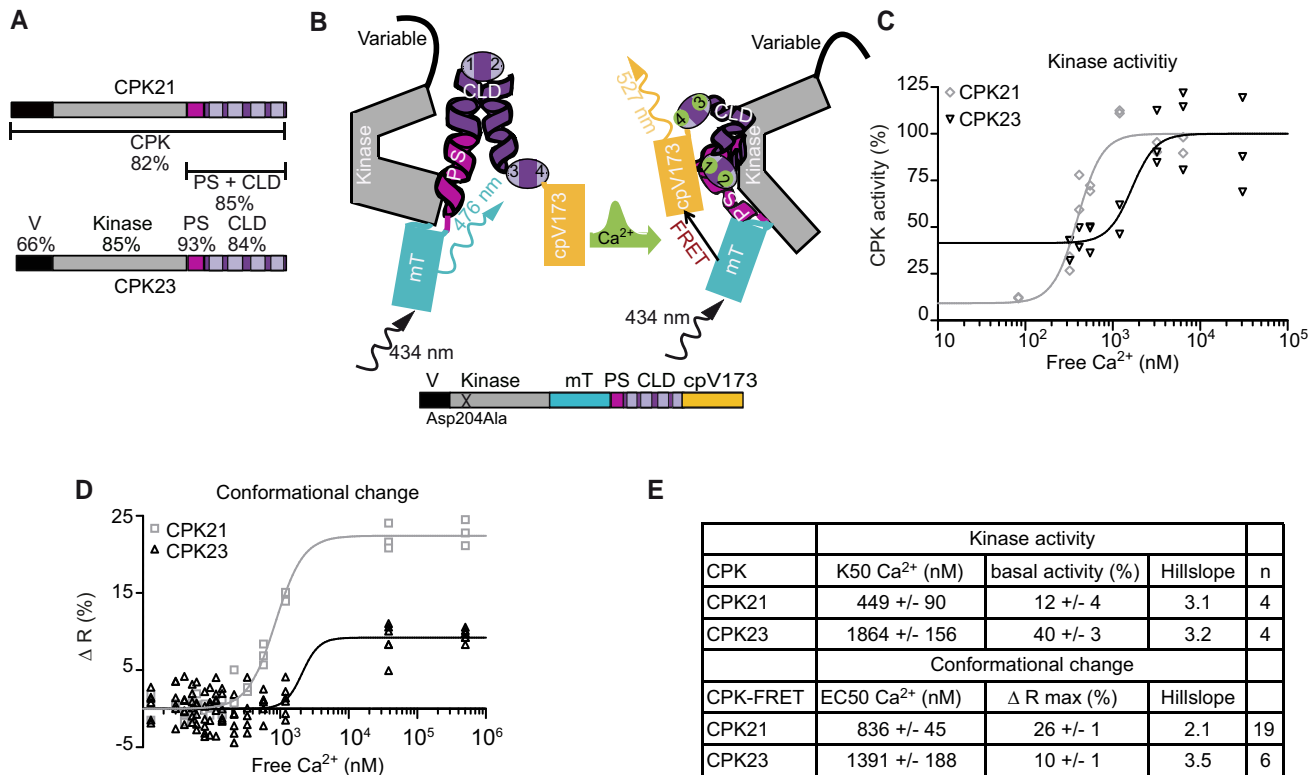
Figure 1. CDPK-FRET reports isoform-specific Ca^{2+}-dependencies of conformational changes of CDPKs. **A)** Schematic diagrams of CPK21 and CPK23 displaying the variable domain (V), kinase domain (Kinase), pseudosubstrate segment (PS) and calmodulin-like domain (CLD) containing four EF-hand motifs (bright boxes). Numbers indicate the percentage of identical amino acids between CPK21 and CPK23. **B)** Schematic diagram of CDPK-FRET, mTurquoise (mT) and cpVenus173 (cpV173) sandwiching CPK PS-CLD. The conformation change in CDPK-FRET following Ca^{2+}-binding is shown in the transition from the left model to the right. Ca^{2+}-binding brings mT and cpV173 into close proximity, allowing for the detection of this conformation change via FRET. **C)** *In vitro* kinase activity using CPK21 and CPK23 proteins expressed and purified from *E. coli* with a peptide of SLAC1 as substrate in the presence of increasing amounts of Ca^{2+} ($R^2_{CPK21} = 0.91$, $R^2_{CPK23} = 0.76$, $K50_{CPK21} = 397$ nM Ca^{2+}, $K50_{CPK23} = 1,656$ nM Ca^{2+}). Activity is expressed as a percentage of activity at full Ca^{2+}-saturation. One representative experiment is shown. For each of the 7 Ca^{2+}-concentrations, purified enzyme was added to 2–3 premixed reaction mixtures resulting in 2–3 technical replicates. **D)** *In vitro* FRET-recorded conformational changes of CPK21- and CPK23-FRET fusion proteins expressed and purified from *E.coli* are plotted against Ca^{2+}-concentration ($R^2_{CPK21} = 0.98$, $R^2_{CPK23} = 0.69$, $EC50_{CPK21} = 857$ nM Ca^{2+}, $EC50_{CPK23} = 2,095$ nM Ca^{2+}). The best fit-value obtained for the bottom or base level of FRET emission ratio was used to calculate changes in emission ratio [ΔR (%)]. Therefore, ΔR is given as the percentage increase in ratio over the base level of FRET emission ratio. One representative experiment is shown. For each of the 15 Ca^{2+}-concentrations, purified CDPK-FRET fusion protein was combined with the corresponding Ca^{2+} buffer at 1:1 dilution in 3–6 technical replicates. **E)** Summary of half-maximal kinase activity (K50) and half-maximal effective concentration (EC50) of conformational change in *n* independent experiments; '*n*' refers to the number of experiments (mean ± SEM). The Hill slope is fitted as a shared value for all data sets of the same enzyme.

genetically encoded FRET biosensor like cameleon, Clomeleon, and ABAleon (Miyawaki et al., 1997, Kuner and Augustine, 2000, Waadt et al., 2014). Using two CDPKs (CPK21 and CPK23) with contrasting Ca^{2+}-sensitivities, we demonstrate that CDPK-FRET pairs genuinely record the Ca^{2+}-dependent conformational change and, thus, reflect kinase activity. We validated our FRET approach in the single cell model system of tobacco (*Nicotiana tabacum*) pollen tubes, which exhibit natural oscillations in Ca^{2+}-concentration during growth. In this system, we were able to show conformational changes of CPK21 that reflect these Ca^{2+}-oscillations, supporting both the notion of a CDPK isoform-specific Ca^{2+}-sensitivity as well as its signal reversibility. Furthermore, in guard cells, both the ABA- and flg22-induced Ca^{2+} signatures induced the conformational

activation of CPK21. Therefore, our technique can be used to monitor real time Ca^{2+}-dependent decoding *in planta*.

Results

A FRET-based sensor records isoform-specific Ca^{2+}-induced conformational changes of CDPKs

The design for a CDPK conformation reporter capable of recording the enzyme's Ca^{2+} binding-dependent conformational change was inspired by structural data from CDPK1 of the parasitic protozoan *Tg*. The X-ray structure of *Tg*CDPK1 reveals a Ca^{2+} binding-mediated conformational change for PS and CLD (Ojo et al., 2010; Wernimont et al., 2010). This caused us to speculate that Arabidopsis CPKs undergo similar conformational changes for their activation, which prompted us to

ask if these changes could be recorded in real-time. To address these questions, we devised a FRET-based approach where we sandwiched PS-CLD between a FRET fluorescent protein pair consisting of mTurquoise (mT) as a donor between the kinase and PS domains, and Venus (circularly permutated at amino acid 173, cpV173) as an acceptor C-terminal to the CLD (Figure 1B). The FRET donor is inserted between the kinase and PS domains because the kinase domain stabilizes the inactive enzyme conformation via interaction with the PS (Wernimont et al., 2010; Wernimont et al., 2011).

To estimate the expected changes in distance between the N-terminus of the PS and the C-terminus of the CLD's fourth EF-hand, the distance in Å was calculated using RasMol (Bernstein, 2009) for active TgCDPK1 and inactive TgCDPK1 3D structure. For TgCDPK1, Ser317 was identified as the first PS amino acid (based on homology to *A. thaliana* PS) and TgCDPK1 Lys502 as the last amino acid of EF-hand 4 (Wernimont et al., 2011); the change in distance between both amino acids was calculated from 55 Å (inactive) to 33 Å (active). Such a decrease in distance was expected to lead to an increase in the emission ratio for a CFP-YFP FRET pair (Zimmermann et al., 2002). For biochemical characterization of CDPKs, all FRET-based CDPK conformation reporters and native CDPKs were expressed and purified as recombinant fusion proteins in *Escherichia coli* (Supplemental Figure S1G). If not otherwise stated, kinase-deficient variants were used for all CDPK-FRET fusion proteins to exclude the influence of auto-phosphorylation on the conformational change. These kinase-deficient variants carry an amino acid substitution in the catalytically critical proton acceptor site for the hydroxyl group of substrates (McClendon et al., 2014).

We first established the FRET-based CDPK conformation reporter for *A. thaliana* CPK21, a highly Ca²⁺-sensitive CDPK with a half-maximal *in vitro* kinase activity (K50) at 449 nM Ca²⁺ (Geiger et al., 2010; Franz et al., 2011; Geiger et al., 2011) (Figure 1C, E). We tested different lengths and sequences of linkers connecting PS and CLD with the fluorophores, plus a deletion variant lacking 8 C-terminal amino acids after the fourth EF hand (Supplemental Figure S1A). All CPK21 conformation reporters, expressed and purified as recombinant fusion proteins, displayed increasing emission ratios with increasing Ca²⁺-concentration and with similar half-maximal effective concentrations (EC50) for Ca²⁺ (Supplemental Figure S1A, C, F). The CPK21-FRET variant with the highest change in emission ratio (26%, F4) was used as a template for other CDPK-based FRET constructs. The deduced EC50 value for the conformational change of CPK21-FRET was 836 nM Ca²⁺ (Figure 1D-E).

To test if the mT insertion between the kinase domain and PS influences kinase activity, we generated an additional CPK21k-FRET variant with an active kinase domain. CPK21K-FRET displayed low auto- and trans-phosphorylation activity and lacked a Ca²⁺-dependent increase in catalytic activity (Supplemental Figure S2 A-B, E). Thus, CDPK-FRET reports the conformational change in CDPK activation but may not monitor all regulatory aspects of biochemical CDPK catalytic activity that involve (auto/trans-) phosphorylation steps.

Because the kinase domain stabilizes the inactive enzyme conformation via interaction with the PS (Wernimont et al., 2010; Wernimont et al., 2011), we analyzed the impact of the kinase domain on the conformational change. We generated a truncated CPK21-FRET variant lacking the N-terminal variable and kinase domain, which is named after the residual CPK21 protein domains PS-CLD21. Remarkably, the PS-CLD21-FRET sensor yielded significant variation in the EC50 values for Ca²⁺-sensitivities (ranging from 200 to 1000 nM) between the different experiments (Supplemental Figure S2 C, E). By contrast, the CPK21-FRET conformation sensor, which we assessed in parallel, showed low variation of the EC50 values (718–975 nM) (Supplemental Figure S2 D-E). We interpret this high variance in the observed conformational change as a lack of intramolecular interaction sites that stabilize the conformation in the PS-CLD protein. This interpretation is consistent with published structural data comparing full length CDPKs with a truncated version encompassing PS-CLD only (Chandran et al., 2006; Wernimont et al., 2011). According to these analyses, in PS-CLD, the PS-helix does not show the correct intramolecular folding into a hydrophobic groove of its own CLD, but instead interacts with the same hydrophobic groove of a dimer protein partner.

Since EF-hands are known to competitively bind to Mg²⁺ in addition to Ca²⁺ (Gifford et al., 2007), we analyzed the emission ratio changes of CPK21-FRET with different concentrations of Mg²⁺. Physiological free concentrations of 0.5–1 mM Mg²⁺ (Saris et al., 2000) decreased the CPK21-FRET energy transfer efficiency only in the absence of Ca²⁺ (Supplemental Figure S1D), indicating binding selectivity for Ca²⁺ over Mg²⁺. An altered CPK21-FRET conformation occurs when binding either Ca²⁺ or Mg²⁺. This binding selectivity for Ca²⁺ is further confirmed by the observation that the standard buffer for *in vitro* FRET conformation measurements includes 10 mM MgCl₂. The Ca²⁺-induced changes in CPK21-FRET were stable over the plant cytosolic pH range of ~7.2–7.5 (Felle, 2001; Zhou et al., 2021) (Supplemental Figure S1E).

Experiments with CPK23 showed a bi-partite pattern for catalytic kinase activity consisting of a Ca²⁺-insensitive basal activity of 40% and an additional Ca²⁺-sensitive increase with low dependency (K50 = 1,864 nM Ca²⁺) (Figure 1C, E). In agreement with this finding, CPK23-FRET reported a modest Ca²⁺-induced change in FRET efficiency of 10%, with a low Ca²⁺-sensitivity (EC50 = 1,391 nM) (Figure 1D-E). Taken together, these data demonstrate that CDPK-FRET conformational change measurements accurately report isoform-specific differences in Ca²⁺-sensitivity for CPK21 compared to CPK23 (Supplemental Figure S3).

CDPK-FRET identifies single amino acid residues as determinants of the Ca²⁺-dependent conformational change

CDPKs are characterized by their isoform-specific and highly variable Ca²⁺ dependencies for the respective kinase activities (Geiger et al., 2010; Geiger et al., 2011; Boudsocq et al.,
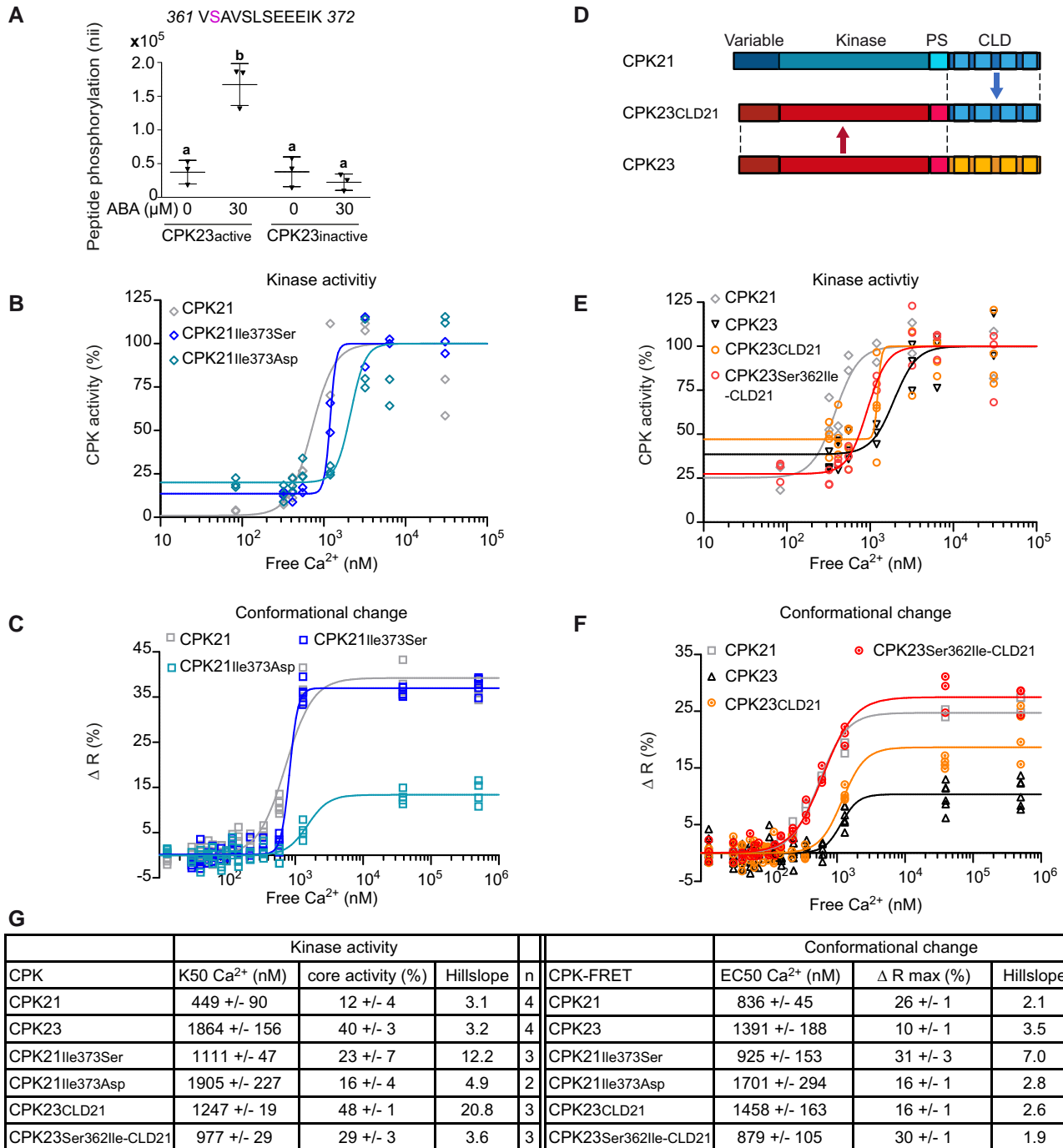
G

CPK	Kinase activity				CPK-FRET	Conformational change			
	K50 Ca^{2+} (nM)	core activity (%)	Hillslope	n		EC50 Ca^{2+} (nM)	Δ R max (%)	Hillslope	n
CPK21	449 +/- 90	12 +/- 4	3.1	4	CPK21	836 +/- 45	26 +/- 1	2.1	19
CPK23	1864 +/- 156	40 +/- 3	3.2	4	CPK23	1391 +/- 188	10 +/- 1	3.5	6
CPK21Ile373Ser	1111 +/- 47	23 +/- 7	12.2	3	CPK21Ile373Ser	925 +/- 153	31 +/- 3	7.0	4
CPK21Ile373Asp	1905 +/- 227	16 +/- 4	4.9	2	CPK21Ile373Asp	1701 +/- 294	16 +/- 1	2.8	5
CPK23CLD21	1247 +/- 19	48 +/- 1	20.8	3	CPK23CLD21	1458 +/- 163	16 +/- 1	2.6	3
CPK23Ser362Ile-CLD21	977 +/- 29	29 +/- 3	3.6	3	CPK23Ser362Ile-CLD21	879 +/- 105	30 +/- 1	1.9	4

Figure 2. A unique single auto-phosphorylation site in the pseudosubstrate segment controls the Ca^{2+}-dependency of the conformational change and kinase activity of CDPKs. **A)** Arabidopsis protoplasts expressing catalytic active or inactive CPK23 were treated with 30 μM ABA or untreated (for the control), and *in vivo* phosphorylation at S362 was quantified via selected reaction monitoring (SRM) mass spectrometry. The CPK23 phosphorylation site is indicated in magenta. Mean ± SD of normalized ion intensities (nii), combining three experiments, are shown as individual data points, $p \leq 0.05$, one-way ANOVA, Tukey's post hoc test; different letters indicate significant differences. **B)** Kinase activity of CPK21 and PS variants carrying an amino acid substitution (CPK21Ile373Ser, CPK21Ile373Asp) plotted against Ca^{2+}-concentrations ($R^2_{CPK21} = 0.85$, $R^2_{CPK21Ile373Ser} = 0.97$, $R^2_{CPK21Ile373Asp} = 0.87$, K50$_{CPK21}$ = 711 nM Ca^{2+}, K50$_{CPK21Ile373Ser}$ = 1,198 nM Ca^{2+}, K50$_{CPK21Ile373Asp}$ = 2,123 nM Ca^{2+}). **C)** FRET-recorded *in vitro* conformational changes of CPK21, CPK21Ile373Ser, and CPK21Ile373Asp plotted against Ca^{2+}-concentrations ($R^2_{CPK21} = 0.96$, $R^2_{CPK21Ile373Ser} = 0.99$, $R^2_{CPK21Ile373Asp} = 0.88$, EC50$_{CPK21}$ = 720 nM Ca^{2+}, EC50$_{CPK21Ile373Ser}$ = 830 nM Ca^{2+}, EC50$_{CPK21Ile373Asp}$ = 1,529 nM Ca^{2+}). **D)** Schematic diagram of CPK23CLD21 chimeras. Abbreviation as in Figure 1A. **E–F)** Kinase activity (**E**) and FRET efficiency (**F**) of CPK21, CPK23, CPK23CLD21, and CPK23Ser362Ile-CLD21, plotted against Ca^{2+}-concentrations (Kinase activity: $R^2_{CPK21} = 0.85$, $R^2_{CPK23} = 0.89$, $R^2_{CPK23CLD21} = 0.69$, $R^2_{CPK23S362I-CLD21} = 0.92$, K50$_{CPK21}$ = 383 nM Ca^{2+}, K50$_{CPK23}$ = 1,942 nM Ca^{2+}, K50$_{CPK23CLD21}$ = 1,237 nM Ca^{2+}; K50$_{CPK23Ser362Ile-CLD21}$ = 928 nM Ca^{2+}; Conformational change: $R^2_{CPK21} = 0.99$, $R^2_{CPK23} = 0.81$, $R^2_{CPK23CLD21} = 0.91$, $R^2_{CPK23Ser362Ile-CLD21} = 0.98$, EC50$_{CPK21}$ = 545 nM Ca^{2+}, EC50$_{CPK23}$ = 1,156 nM Ca^{2+},

(continued)

2012). To further assess the power and resolution of CDPK-FRET, we employed the CDPK-FRET reporter to resolve the molecular basis for the contrasting Ca^{2+}-sensitivities of CPK21 and CPK23. A comparison of the primary amino acid sequences from these closely related enzymes (Figure 1A) identified a conserved hydrophobic amino acid, isoleucine, at PS position 31 in CPK21 (Ile373). A hydrophobic amino acid is present at PS position 31 in the entire *A. thaliana* CDPK family, except in CPK23, where it is replaced by serine (Ser362) (Supplemental Figure S4A). CDPK phosphorylation motifs are often encompassed by basic amino acids N-terminal to phosphorylated Ser/Thr; such a cluster of basic amino acids is present N-terminal to Ser362 (Huang et al., 2001). Indeed, upon transient expression in Arabidopsis protoplasts, an (auto)-phosphorylated Ser362-containing peptide was detected in response to 30 µM ABA when cells were transfected with active CPK23, but not with a kinase-deficient CPK23 variant (Figure 2A, Supplemental Figure S4B-C). CPK23 auto-phosphorylation at Ser362, in a Ca^{2+}-independent manner, was verified by *in vitro* kinase assays using recombinant GST-His-tagged CPK23 purified from *E. coli* and analyzed by targeted mass spectrometry (Supplemental Figure S5).

To examine the importance of Ile373 (CPK21) and Ser362 (CPK23) for Ca^{2+}-sensitivity, we tested CPK derivates with amino acid substitutions in these positions for their impact on Ca^{2+}-sensitivity in terms of both kinase activity and conformational changes. In CPK21, we generated substitutions at Ile373 for Ser (as in CPK23) and Asp (mimicking auto-phosphorylated CPK23). In kinase assays, CPK21 substitutions Ile373Ser and Ile373Asp caused an increase in the K50 value from 449 nM (WT) to 1,111 nM (Ile373Ser) and 1,905 nM (Ile373Asp) free Ca^{2+}, respectively. The respective basal activity also changed from 12% (WT) to 23% (Ile373Ser) and to 16% (Ile373Asp) (Figure 2B, G). In the corresponding CPK21-FRET conformational change measurements, an increase of the EC50 value from 836 nM (WT) to 925 nM (Ile373Ser) and to 1,701 nM (Ile373Asp) free Ca^{2+} was observed. The respective maximal FRET efficiency changed from 26% (WT) to 31% (Ile373Ser) and to 16% (Ile373Asp) (Figure 2C, G). Of note, in the case of Ile373Ser, the effect of the amino acid exchange on Ca^{2+}-sensitivity in terms of conformational change was rather small (Supplemental Figure S3B). This may be due to the loss of

auto-phosphorylation capacity in Ile373Ser-CDPK-FRET. These data indicate that a single amino acid exchange reduces Ca^{2+}-sensitivity compared to native CPK21 and, even more importantly, the Ca^{2+}-sensitivity of CPK21Ile373Asp resembles the Ca^{2+}-sensitivity of CPK23. Also, these data verify that CDPK-FRET reports Ca^{2+} dependencies at a similar resolution to catalytic activity measurements.

Conversely, in CPK23, the substitution Ser362Ile (K50 = 1,231 nM) rendered the enzyme more sensitive to Ca^{2+} in kinase assays, while Ser362Asp led to constitutive Ca^{2+} insensitive activity (Supplemental Figure S4F-G). Interestingly, when using CPK23-FRET, both introduced amino acid substitutions resulted in comparable, weak signals for conformational change, with Ca^{2+} dependencies comparable to that of the native CPK23 protein (Supplemental Figure S3B, S4D, G). In these specific experiments, the kinase-active form of CPK23K-FRET was used to enable auto-phosphorylation at Ser362, whereby the active and inactive CPK23-FRET variants displayed similar EC50 values and FRET efficiencies (Supplemental Figure S4E, G).

To exclude the possibility that the comparatively low FRET efficiency of CPK23 masks subtle conformational changes, we conducted a CLD domain swap from CPK21 to CPK23 (Figure 2D). Chimeric CPK23CLD21-FRET showed increased maximal FRET efficiency (Figure 2F), indicating altered (higher) distance changes between the donor and acceptor. The (low) Ca^{2+}-sensitivity of CPK23CLD21-FRET was comparable to that of native CPK23-FRET. Remarkably, increased Ca^{2+}-sensitivity was observed for CPK23Ser362Ile-CLD21-FRET, displaying a Ca^{2+}-dependent conformational change indistinguishable from that of CPK21 (Figure 2F, Supplemental Figure S3B). Also, when looking at kinase activity, CPK23CLD21 showed an increase in Ca^{2+}-sensitivity (K50 = 1,247 nM) compared to CPK23 (K50 = 1,864 nM), and CPK23Ser362Ile-CLD21 (K50 = 977 nM) showed a greater increase in Ca^{2+}-sensitivity (Figure 2E, G). Taken together, these data uncover a single CPK23 auto-phosphorylation site, Ser362, as key to modifying Ca^{2+}-sensitivity and shifting catalytic activity. In addition, we validated CDPK-FRET as a powerful tool to assess the biochemical properties of CDPKs using the activation step, the Ca^{2+} binding-dependent conformational change, as a molecular readout.

Figure 2. (Continued)
EC50$_{CPK23CLD21}$ = 1,200 nM Ca^{2+}; EC50$_{CPK23Ser362IleCLD21}$ = 629 nM Ca^{2+}). **B, E** Kinase assays performed using recombinant GST-His-tagged enzymes expressed and purified from *E. coli* with a SLAC1 peptide as a substrate including the CDPK *in vivo* phosphorylation site (SLAC1 Ser59). Kinase activity is expressed as a percentage of activity measured at saturating Ca^{2+}-concentration (2–3 technical replicates for each of the 7–8 Ca^{2+}-concentrations). FRET-imaged conformational changes of recombinant CDPK-FRET fusion proteins expressed and purified from *E. coli* (**C, F**). Conformation changes are expressed as percent increase in ratio over the base level of FRET emission ratio (3–6 technical replicates for each of the 14–15 Ca^{2+}-concentrations). **G)** Summary of half-maximal kinase activity (K50) and half-maximal effective concentration (EC50) of conformational change in *n* independent experiments; '*n*' refers to the number of experiments (mean ± SEM). The Hill slope is fitted as a shared value for all data sets of the same enzyme. Summary encompasses all measurements per construct; therefore, values for the same construct are identical in different figures.
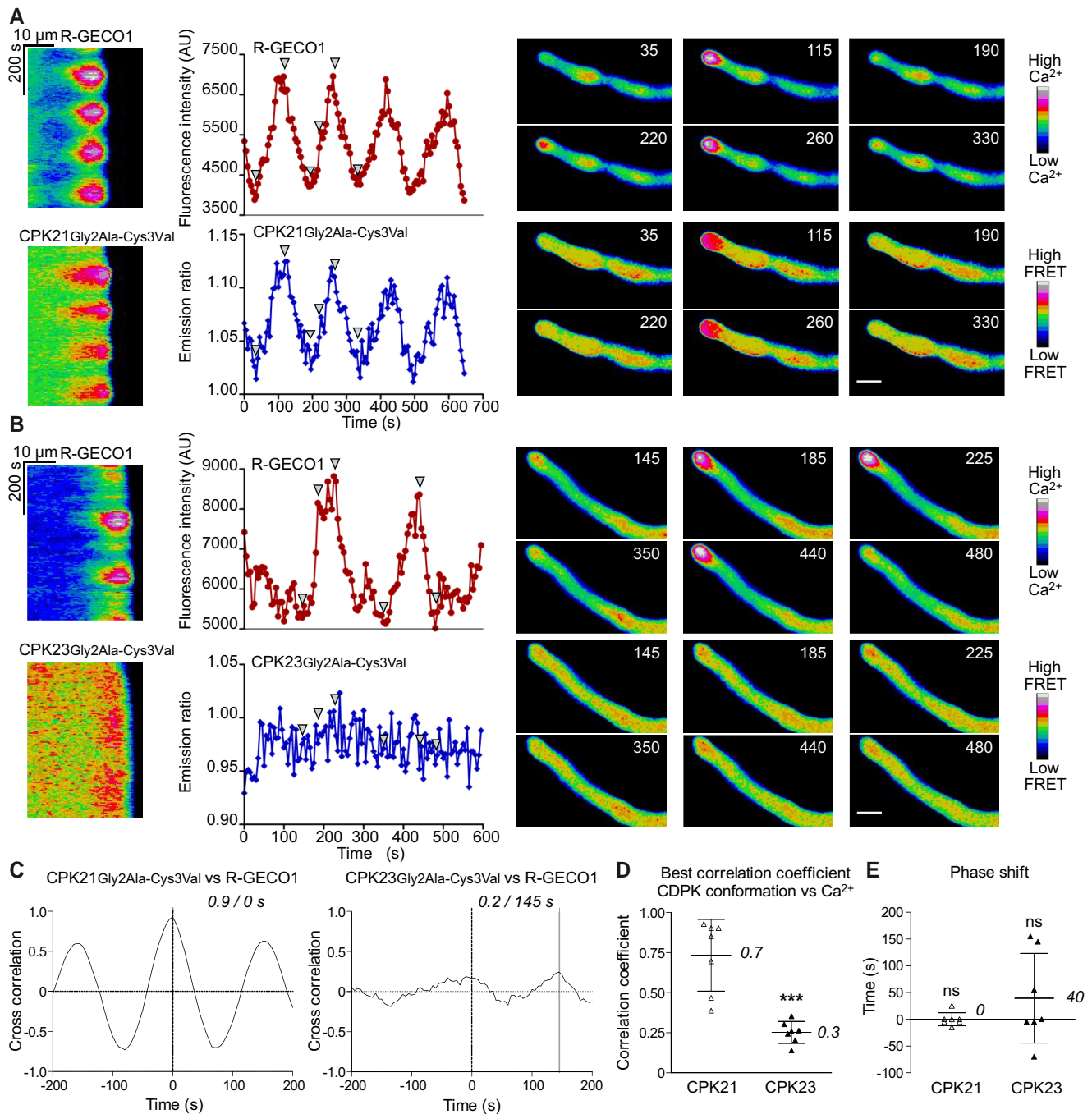
Figure 3. Tobacco pollen tube tip-focused Ca²⁺-oscillations are decoded in real-time by CPK21-FRET but not by CPK23-FRET. **A, B)** Tobacco pollen tubes carrying the R-GECO1 Ca²⁺-sensor as a stable transgene were transiently transformed with CDPK-FRET reporters CPK21Gly2Ala-Cys3Val (**A**) or CPK23Gly2Ala-Cys3Val (**B**). Growing pollen tubes were imaged in parallel for cytosolic changes in Ca²⁺-concentrations (top graphs, red) and CDPK conformational change (lower graphs, blue). Representative experiments are shown (in total $n = 7$ transfected pollen tubes per construct, > 4 independent transient transformations). Ca²⁺-oscillations were induced using a medium containing 10 mM Cl⁻. Images were taken every 5 s for 650 s (**A**) and 595 s (**B**). Results are presented both as kymographs and as intensity-over-time-plots for quantification. Fluorescent signals were quantified ∼ 5–15 μm behind the tips of growing pollen tubes. Values in CDPK-FRET kymographs and example pollen tubes images were calculated by dividing the CFP excitation/YFP emission image by CFP image using Fiji. Arrowheads in the intensity plots correspond to the false colored pollen tube images shown on the right side. The time stamp (s) is visible in the top right of pollen tube images and the scale bar is 15 μm. **C)** Synchronization analysis between cytosolic Ca²⁺-concentration and CDPK conformational change in pollen tubes. The correlation co-efficient between the R-GECO1 and CDPK-FRET signals is plotted for time delays of −200 s to +200 s (CPK21 left panel, corresponding to 3**A**; CPK23, right panel, corresponding to 3**B**). A solid grey line marks the time delay with the highest correlation coefficient, which is indicated above the graph. The phase relationship between the signals is indicated as time difference in seconds. Time < 0 corresponds to leading, time > 0 to lagging

CDPK-FRET mirrors the cytosolic Ca^{2+} oscillatory pattern during pollen tube growth

Next, we aimed to use CDPK-FRET in an environment of changing Ca^{2+}-concentrations in a plant cell system. Growing pollen tubes are an optimal single cell model system for cytosolic Ca^{2+} imaging, as they are characterized by a tip-focused standing gradient with frequent, well defined, Ca^{2+}-oscillations (Michard et al., 2008; Konrad et al., 2011; Damineli et al., 2017; Michard et al., 2017; Li et al., 2021). We generated cytosolic CDPK-FRET variants by deleting the myristoylation Gly2Ala and palmitoylation Cys3Val sites. To increase the brightness of the FRET donor in *in vivo* imaging experiments, we replaced mT with eCFP (cyan fluorescent protein) without altering the kinetics of conformational change (Supplemental Figure S1B, F). These cytosolic CDPK-FRET variants were transiently expressed in tobacco pollen expressing the cytosolic Ca^{2+} sensor R-GECO1 as a stable transgene (red fluorescent genetically encoded Ca^{2+} indicator for optical imaging) (Zhao et al., 2011). CDPK-FRET and R-GECO1 signals were recorded simultaneously by time-lapse imaging of the transfected pollen. Both sensors localize to the cytosol, ensuring that subcellular differences in Ca^{2+} dynamics would not influence the comparison. Tip-focused, dynamic, cytosolic Ca^{2+}-oscillation patterns were provoked using a medium containing 10 mM Cl$^-$ (Gutermuth et al., 2013). Importantly, cytosolic Ca^{2+}-concentrations in tobacco pollen tubes have already been quantified (Michard et al., 2008) and were found to change from 0.1–0.2 to >1.0 µM from the shank to the tip. These cellular settings allowed us to estimate the Ca^{2+} changes sensed by the CPK21- and 23-FRET pairs with their distinct Ca^{2+}-sensitivities (Figure 1E).

Accordingly, CPK21-FRET pollen displayed changes in emission ratios, which closely reflected the tip-focused cytosolic Ca^{2+} patterns in terms of amplitude, phase, and shape, showing the rapid reversibility of the CPK21 conformational change (Figure 3A and Supplemental Figure S6, Movie 1). A high correlation coefficient (0.7 ± 0.2, Figure 3C-D) was obtained in synchronization analyses between the cytosolic Ca^{2+}-concentration monitored by R-GECO1 and the CDPK-FRET-monitored conformational change of CPK21. By contrast, CPK23-FRET was unable to monitor any tip-focused oscillatory cytosolic Ca^{2+}-concentration pattern; this is consistent with the low Ca^{2+}-sensitivity of CPK23 kinase activity and the small conformational changes (Figure 3B, Supplemental Figure S7, Movie 2). This finding is consistent with the weak correlation between Ca^{2+} changes and CPK23-FRET signal changes (correlation

coefficient of 0.3 ± 0.1) (Figure 3C-D). In conclusion, cytosolic CPK21-FRET captures the oscillatory Ca^{2+}-concentration pattern in pollen, in phase, and without a significant time delay (Figure 3D-E), thus demonstrating that it is a fast and accurate reporter/sensor of Ca^{2+} changes.

CPK21-FRET identifies functional stress-specific Ca^{2+} decoding in guard cells

Guard cells respond to the application of either ABA or flg22, often with cytosolic Ca^{2+} changes, which are relayed via different Ca^{2+} sensor kinases to the anion channels that initiate stomatal closure (Thor and Peiter, 2014; Brandt et al., 2015; Guzel Deger et al., 2015; Keinath et al., 2015; Huang et al., 2019; Li et al., 2021). To test if CPK21 is biochemically activated in response to one or both stimuli, we generated stable Arabidopsis lines in the Col-0 R-GECO1 background (Waadt et al., 2017) expressing plasma membrane localized CPK21-FRET (Figure 4, Supplemental Figure S8B) under the control of a ß-estradiol-inducible promoter. After the application of 20 µM ABA or 100 nM flg22 to epidermal peels, CPK21-FRET and R-GECO1 signals were recorded simultaneously by time-lapse imaging of selected single guard cells.

Both stimuli induced an increase in cytosolic Ca^{2+}-concentrations in the form of repetitive transients in the R-GECO1 signal, which is indicative of distinct Ca^{2+} signatures. A higher maximum Ca^{2+} signal change was observed upon flg22 treatment than ABA (Figure 4, Figure 5A). Remarkably, both ABA and flg22 also triggered a conformational change in CPK21, as recorded by CPK21-FRET. Thus, CPK21 activation is not only triggered by ABA, as one may have presumed (Geiger et al., 2010; Geiger et al., 2011), but also by flg22 (Figure 4, Supplemental Figure S8, S9, S10). Synchronization analysis showed that for both stimuli, the changes in Ca^{2+}-concentration and the respective CPK21 conformational changes are linked (correlation coefficient: ABA $= 0.6 \pm 0.1$, flg22 $= 0.7 \pm 0.1$, Figure 4, 5B). However, detailed evaluation of the Ca^{2+} signatures (curves shown in red) in relation to the signal curves for FRET-monitored CPK21 conformational changes (shown in blue) uncovered stimulus-specific differences in the decoding of Ca^{2+} by CPK21. Importantly, in contrast to the analysis in pollen, where CPK21-FRET and R-GECO1 recorded almost identical kinetics and spatiotemporal patterns (Δarea $6 \pm 7\%$, $n = 3$; Supplemental Figure S11), in the biological context of guard cells, differences between Ca^{2+}-concentration change and CPK21 conformational change kinetics are apparent (Figure 5C, blue shaded area in Figure 5E-F).

Figure 3. (Continued)
R-GECO1 (Ca^{2+}-concentration) signals compared to CDPK-FRET signal changes, and 0 indicates no delay. **D, E)** Summary of synchronization analysis correlation coefficients (**D**) or time delay for the most probable match (in seconds) (**E**) are shown. Data represent the mean $\pm$ SD (numbers represent means), and dots represent the individual measurements ($n = 7$). **D)** *t*-test yields a significant difference *** $p \leq 0.001$ between correlation coefficients of either CPK21 or CPK23 conformational change to Ca^{2+}-concentration. **E)** One-sided *t*-test reveals no significant differences (ns, $p \leq 0.05$) from zero.
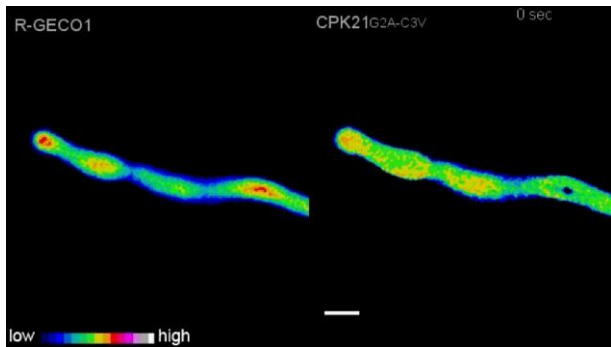
Movie 1. Tip-focused intracellular Ca^{2+} gradient and Ca^{2+}-oscillations in a growing tobacco pollen tube expressing CPK21Gly2Ala-Cys3Val-FRET. Tobacco pollen carrying the R-GECO1 Ca^{2+}-sensor as a stable transgene were transiently transformed with CDPK-FRET conformational change sensors containing CPK21Gly2Ala-Cys3Val-FRET. Time-dependent fluorescence intensity changes induced by a medium containing 10 mM Cl^{-} were recorded as a time-laps video. The time-laps video represents the same pollen tube as shown in Figure 3A. The images were taken every 5 s for 650 s, assembled as a stack and converted into a video (10 frames/s, 1 s in the video equals to 50 s in the recording, scale bar 15 μm).

Interestingly, quantification of the differences in the 'area under the curve' (AUC) between the plots of Ca^{2+}-concentration changes and CPK21-FRET signal changes (blue shaded area in Figure 5E-F) revealed a statistically significant higher Δarea for flg22 ($46 \pm 10\%$) than for ABA ($34 \pm 10\%$) (Figure 5D). Furthermore, a longer lag time was observed between stimulus application and the appearance of the first Ca^{2+} peak maximum for flg22 (7.8 ± 3.1 min) than for ABA (3.9 ± 1.3 min), and an additional short delay occurred before the first CPK21-FRET recorded peak maximum (Figure 5H). Time differences between the R-GECO1 and CDPK-FRET signal phase revealed that cytosolic Ca^{2+} changes precede the CPK21 conformational changes by ~ 8 s for both treatments (Figure 5G). This time delay from the change in Ca^{2+}-concentration to the change in CPK21 conformation is most prominent for the first peak, corresponding to the initiation of Ca^{2+} signaling, and decreases during subsequent repetitive Ca^{2+} transients (peak2, peak3) (Figure 5I). Taken together, our data visualizing CPK21-mediated Ca^{2+} sensing and induced conformational changes upon ABA- and flg22-treatment in guard cells suggest that CPK21 is a stimulus-specific decoder of distinct Ca^{2+} signatures.

Discussion

CDPKs are important components of the plant Ca^{2+} regulatory signaling network in response to abiotic and biotic stress and during various developmental processes (Boudsocq et al., 2010; Geiger et al., 2010; Geiger et al., 2011; Gutermuth et al., 2013; Matschi et al., 2013; Brandt et al., 2015; Liu et al., 2017; Gutermuth et al., 2018; Durian et al., 2020; Fu et al., 2022). One key question is how members of

the CDPK family are differentially activated and confer distinct signaling functions within a single cell. In this study, we developed a FRET-based reporter for the Ca^{2+}-induced conformational change in CDPK, the CDPK activation step, which precedes ATP-dependent trans-phosphorylation. Thus, in the biological context, CDPK-FRET may visualize the spatial and temporal kinetics of Ca^{2+}-dependent conformational changes as a proxy for CDPK activation and function. The CDPK-FRET reporter monitors Ca^{2+}-dependent conformational changes of the enzyme, whereby a fluorescent protein pair flanks the Ca^{2+} regulatory unit of CDPKs in one fusion protein (Figure 1). This is in contrast to substrate-based protein kinase FRET reporters, where the substrate protein is sandwiched between a fluorescent protein pair (Brumbaugh et al., 2006; Depry and Zhang, 2011; Zaman et al., 2019; Zhang et al., 2020). CDPKs form a multi-protein family for which partially redundant *in vivo* functions and overlapping phosphorylation of identical substrate proteins have been reported (Geiger et al., 2010; Geiger et al., 2011; Gutermuth et al., 2013; Brandt et al., 2015; Liu et al., 2017; Gutermuth et al., 2018). Thus, a substrate-based FRET reporter may not yield an isoform-specific resolution for CDPKs *in planta*. By contrast, Ca^{2+}-dependent conformational changes characterized by K50 and EC50 values are isoform-specific. In addition, regarding the highly conserved modular structure of CDPKs, the CDPK-FRET reporter system established here can be applied to other CDPK isoforms. Our *in vitro* and *in vivo* measurements demonstrated that CPK21 shows Ca^{2+}-sensitivity, with an *in vitro* EC50 of 836 nM, thus suggesting that a significant Ca^{2+}-induced conformational change occurs at physiological cytosolic Ca^{2+}-concentrations (Figure 3, Figure 4). In comparison, the closest homologue, CPK23, follows a different pattern, which includes the unique (ABA-dependent) auto-phosphorylation at Ser362 within its PS domain (Figure 2). The Ser362Asp substitution (phospho-mimic) leads from low Ca^{2+}-sensitivity to a constitutive and entirely Ca^{2+} insensitive activity (Supplemental Figure S4). Such a phospho-Ca^{2+}-sensitivity switch is reminiscent of *A. thaliana* CPK28, where an intrinsic auto-phosphorylation site at Ser318, within the kinase domain, was shown to prime for Ca^{2+}-sensitivity of kinase activity and conformational change (Bender et al., 2017; Bredow et al., 2021). These data provide evidence that (auto-) phosphorylation can influence CDPK Ca^{2+}-sensitivity, and both mechanisms may be linked to the regulation of CDPK function in decoding biological Ca^{2+} signatures *in planta*.

Stimulus-specific encoding of Ca^{2+} signals and signatures depends on the triggering cue and may be generated at subcellular loci within a cell, as determined by the locations of stress cue perception and Ca^{2+} influx channels. Thus, appropriate Ca^{2+} decoding is expected within a spatial overlapping region. Interestingly, Ca^{2+}-oscillations in the pollen single cell system show a synchronous recording of R-GECO1 and CPK21-FRET without shifts in phase. The native *CPK21* gene is not expressed in pollen (Winter et al., 2007), and consistent with this observation, no biological function for
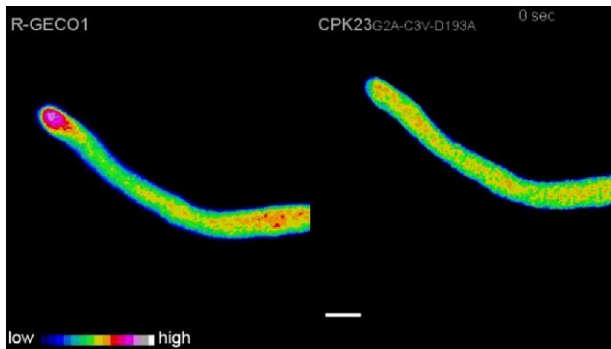
Movie 2. Tip-focused intracellular Ca^{2+} gradient and Ca^{2+}-oscillations in a growing tobacco pollen tube expressing CPK23Gly2Ala-Cys3Val-FRET. Tobacco pollen carrying the R-GECO1 Ca^{2+}-sensor as a stable transgene was transiently transformed with CPK23Gly2Ala-Cys3Val-FRET. Tip-focused dynamic Ca^{2+}-oscillation patterns were induced by using a medium containing 10 mM Cl$^-$. The time-laps video represents the same pollen tube as shown in Figure 3B. The images were taken every 5 s for 595 s, assembled as a stack and converted into a video (10 frames/s, 1 s in the video equals to 50 s in the recording, scale bar 15 μm).

CPK21 has been reported in pollen. In this context, the use of CPK21 lacking its plasma membrane binding motifs, resulting in cytosolic localization, causes CPK21-FRET to behave just like the R-GECO1 Ca^{2+} sensor. In guard cells, the unmodified N-terminal domain of the CPK21-FRET variant controls CPK21-specific localization at the plasma membrane (Demir et al., 2013; Gutermuth et al., 2013; Simeunovic et al., 2016). We expect that in this *in vivo* context, only those fractions of CDPK enzymes that are activated in a time-specific and intracellular spatially distinct manner can perceive appropriate Ca^{2+} changes. CPK21-FRET reports ABA- and flg22-induced Ca^{2+} sensing and conformational changes in guard cells, suggesting that CPK21 functions as a Ca^{2+} decoder that also regulates SLAC1 anion channel activity by phosphorylation (Geiger et al., 2010).

In a biological context, the repetitive Ca^{2+} transients and CPK21-FRET curves indicating the conformational change of CPK21 differed between ABA and flg22 treatments, with a higher signal change dynamic ('AUC') for the latter (Figure 5C-F). Synchronization analyses revealed that the R-GECO1-reported Ca^{2+} changes precede the CPK21 conformational changes by ∼ 8 s for both treatments (Figure 5G). These differences in response times between both signals may reflect differences in sensor/reporter localization. R-GECO1 and the more frequently used ratiometric variant R-GECO1-mT are present in the cytosol and (lacking a nuclear export sequence) partly in the nucleus (Keinath et al., 2015; Waadt et al., 2017) (Supplemental Figure S8B). The analyzed regions of interest (ROIs) in guard cells, in contrast to those in pollen tubes, also encompasses the nucleus. Thus, in guard cells, we combined a cytosolic and nuclear Ca^{2+} sensor (R-GECO1) with a plasma membrane localized CDPK conformation reporter (CPK21-FRET)

(Supplemental Figure S8B). A recent study using differentially localized sensors showed that the times between Ca^{2+} influx at the plasma membrane and Ca^{2+}-changes in the cytosol and nucleus may differ in a stress-dependent manner, indicating specific spatiotemporal Ca^{2+} dynamics (Guo et al., 2022). Remarkably, we observed high synchronization for the Ca^{2+} increase phase, corresponding to rapid Ca^{2+}-induced CDPK activation for both stimuli (Figure 5E-F). By contrast, particularly in response to flg22, the reset of enzyme conformation (as a proxy for enzyme inactivation) was delayed compared to the rapid Ca^{2+} decrease. This stimulus-specific delay in CDPK-FRET reset may represent a read-out for prolonged Ca^{2+} decoding capacity of the CDPK, which in a functional context is translated into enhanced phosphorylation of substrate proteins. Mechanistically, such a delay in reset may be due to post-translational modifications (such as [auto-] phosphorylation) that influence CDPK conformation and activity or a lower Ca^{2+} dissociation rate for CPK21-FRET than for R-GECO1. A CDPK may change its assembly within protein complexes or membrane sub-domains. For example, a stress-dependent delocalization of CPK21 in plasma membrane nanodomains coinciding with the CPK21-SLAH3 interaction has been reported (Demir et al., 2013). Furthermore, the differences in response times and synchronization between cytosolic Ca^{2+} (as reported by R-GECO1) and conformational signals at the plasma membrane (as detected by CPK21-FRET) may reflect the spatial separation and kinetics of extracellular Ca^{2+} influx and the subsequent sequestration of Ca^{2+} into internal stores.

In this study, we established CDPK-FRET and applied it to investigate Ca^{2+}-dependent conformation activation in guard cells. The use of an estradiol-inducible promoter led to a high expression level of the FRET-reporter and ensured a signal-to-noise ratio suitable for detecting sensor signal changes. CDPK-FRET imaging in different cell types for different isoforms may be limited by expression level, with low levels being insufficient for FRET imaging, particularly when using a native promoter. A transfer of CDPK-FRET to other CPDK isoforms may require fine-adjustments in the linker regions to the fluorophore proteins. Also, whereas in this study, CDPK-FRET imaging was applied to a CDPK isoform with a K50 value in the nM range, the suitability of this approach for isoforms with K50 values in a higher μM range remains to be assessed. Finally, the conformational change visualized by CDPK-FRET supports the identification of CDPK activation and function in a specific signaling pathway. Yet, to verify a CDPK as a genuine Ca^{2+} decoder, further validation of the translation process into pathway-specific responses by biochemical and genetic analysis will be required.

Our work introduces a CDPK-FRET tool named CPKaleon as a genetically encoded biosensor for CDPK conformational activation. CPKaleon is a powerful approach for visualizing and understanding real-time Ca^{2+} signaling and decoding in plant cells. In light of the increasing number of characterized ion channel types and non-canonical membrane-permeable proteins of overlapping function in Ca^{2+} influx,
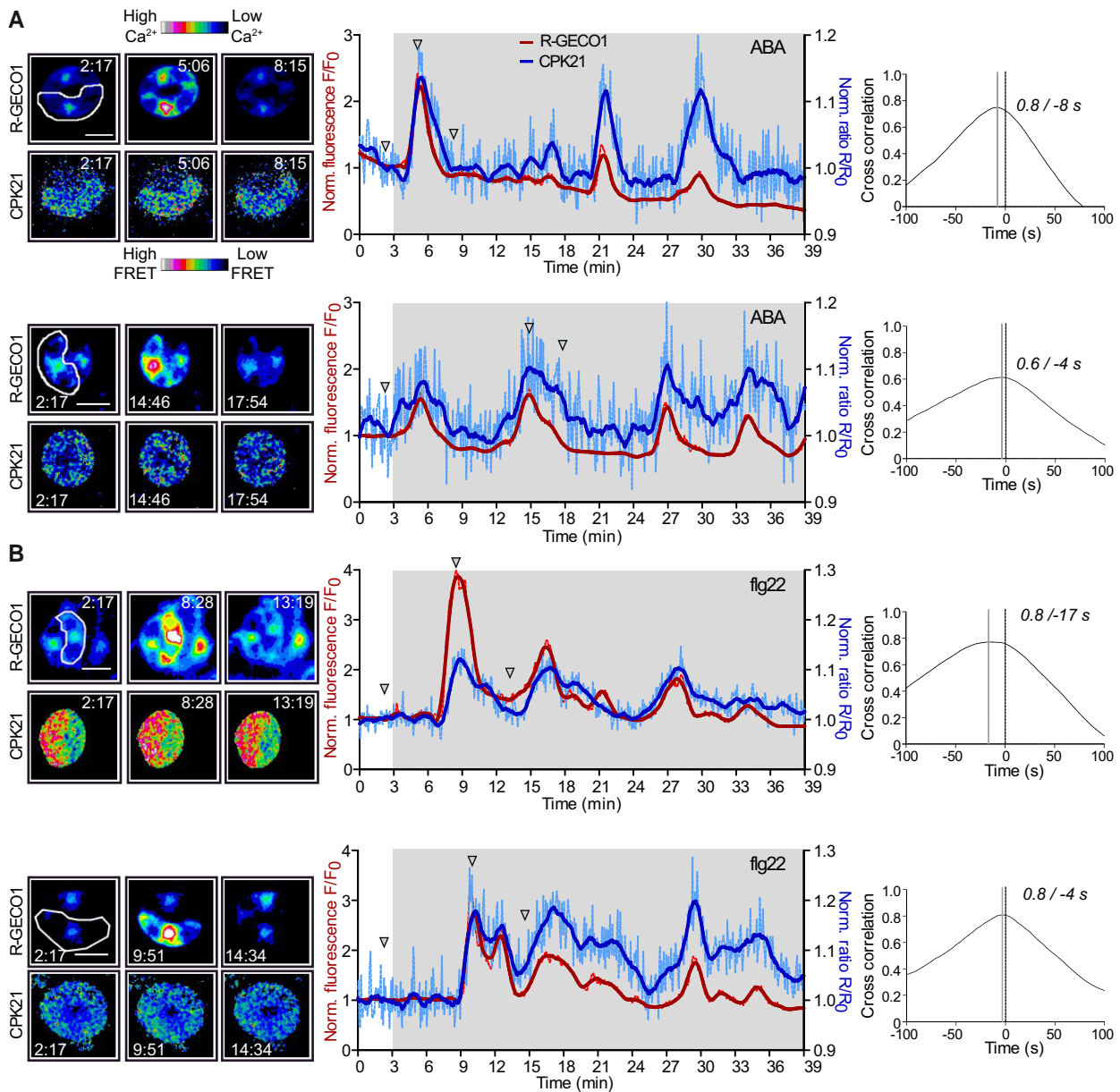
Figure 4. ABA- and flg22-induced changes in Ca^{2+}-concentrations in Arabidopsis guard cells induce real-time conformational activation of CPK21-FRET. **A, B)** Concurrent imaging of changes in cytosolic Ca^{2+} flux (red curve) and FRET ratio (blue curve) in response to 20 µM ABA (**A**) or 100 nM flg22 (**B**). Epidermal peels from estradiol-inducible CPK21-FRET and a constitutive R-GECO1 expressing line were pre-treated with estradiol for 14 to 16 h. Representative experiments are shown ($n \geq 7$ guard cells from 7 plants). Fluorescence images of the guard cells measured (left panels) are shown. Fluorescence images of the CPK21 conformation sensor were calculated via dividing the CFP excitation/YFP emission image by CFP image using Fiji. Continuous lines in intensity-over-time plots (middle panels) represent smoothed fluorescence intensity data (averaging 15 values on each side using a second order polynomial), and dotted lighter colored lines represent normalized, original data. Images were taken every 4.16 s. The underlying grey area indicates the time interval of recording after ABA or flg22 treatment at 3 min. Micrographs represent selected time points, as indicated by arrowheads in the intensity plots. Time stamps are in the format mm:ss, and scale bars are 10 µm. The regions of interest (ROIs) used to measure signal intensity changes are framed white (leftmost panel). Quantification of phase relationships via cross correlation from ABA-treated (**A**) and flg22-treated (**B**) guard cells are shown in the right-hand panels. Synchronization analyses are based on adjusted signal changes (adjusted for signal decreases derived from technical artefacts), calculated by dividing normalized signals by the trend line. The artificial trend line was calculated as linear regression of all data points. The correlation coefficient between the R-GECO1 and CDPK-FRET signals is plotted for time delays of −100 s to +100 s. A solid grey line marks the time delay with the highest correlation coefficient. Time differences between the solid grey and dotted vertical (0 s) lines correspond to leading (shift to left side) R-GECO1 signals. Time delay and highest correlation coefficient are indicated.
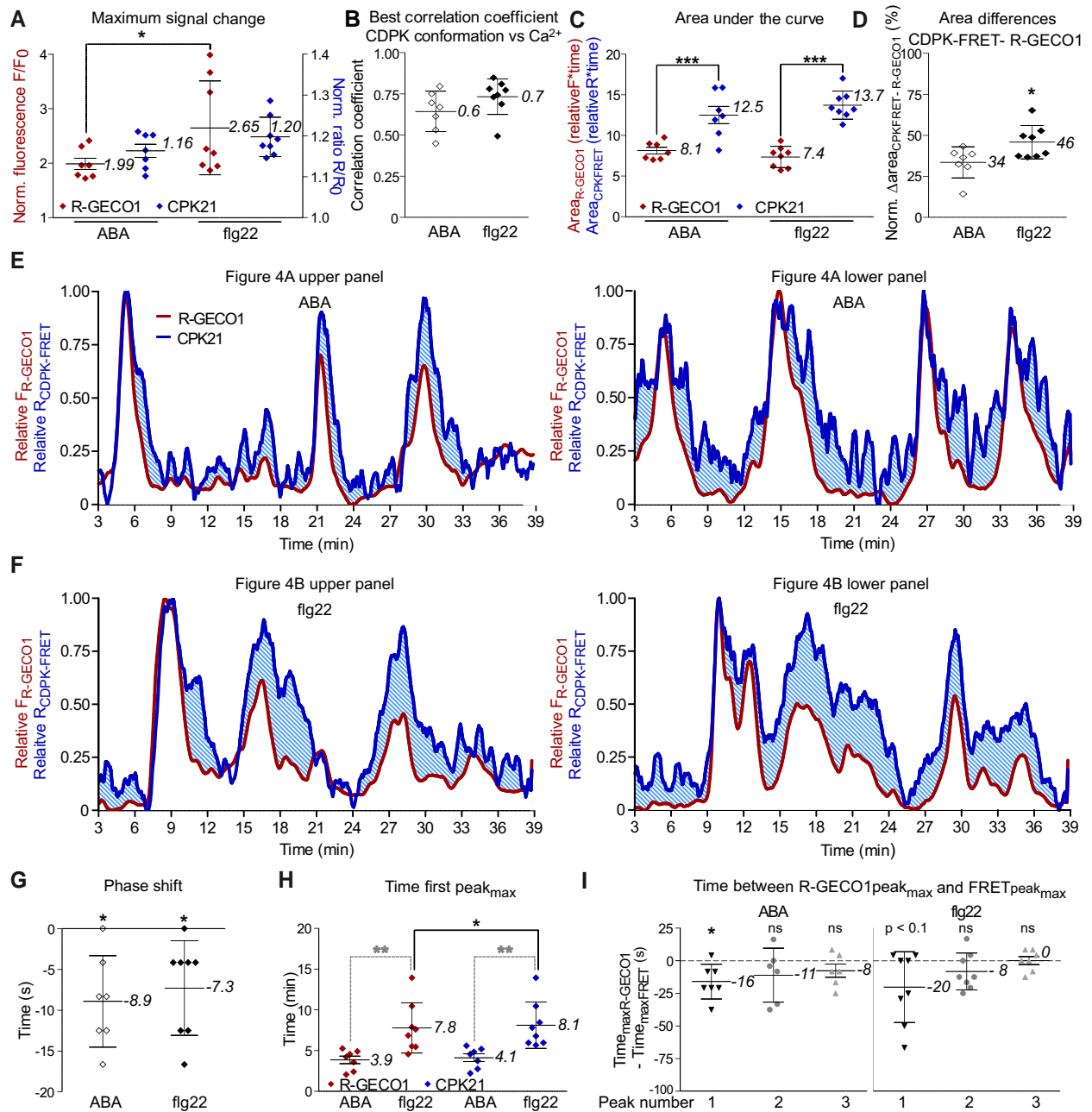
Figure 5. ABA- and flg22-induced CPK21 conformational change signals differ in time, synchronization, strength and shape, indicating stimulus-dependent Ca²⁺ signal decoding. Data from guard cells ($n \geq 7$) of 7 plants expressing the estradiol inducible CPK21-FRET conformation sensor and constitutive expressed R-GECO1 (Ca²⁺-sensor), treated with ABA or flg22. **A, B)** Maximal signal changes (**A**) and correlation coefficients between R-GECO1 and CPK21-FRET signals (**B**). Adjustment of normalized signal (used in analyses **B, E, F**) as described in Figure 4. Significant difference between treatments indicated by '*' ($p \leq 0.05$; two-way ANOVA and Bonferroni post hoc test). **C–F)** Evaluation of decoding by comparative assessment of signal signature (shape of the curves and areas under the curves) from relative signals. For relative signals, the signal minimum was set to zero and the maximum to one (**E, F**). **C)** Significant differences between CPK21-FRET and R-GECO1 are indicated with '***' ($p \leq 0.001$; two-way ANOVA and Bonferroni post hoc test). **D)** By subtracting area$_{R-GECO1}$ from area$_{CPK21-FRET}$, 'area differences' are calculated (Δarea, light blue shaded area in **E, F**). Δ area is normalized to area$_{CPK21-FRET}$. Statistical significance between treatments is indicated by '*' ($p \leq 0.05$; t-test). **G)** Synchronization analysis-derived time delays. In synchronization analysis, R-GECO1 and CPK21-FRET signal changes are shifted relative to each other to determine the time differences that lead to the highest level of correlation (phase shift). The phase shift between the signals is indicated as time difference in seconds. Time < 0 corresponds to leading signals, time > 0 to lagging R-GECO1 signals (Ca²⁺-concentration) compared to CPK21-FRET signal changes, and 0 indicates no delay. Significant differences from 0 are marked '*' ($p \leq 0.05$; one sided t-test). **H)** Time until first peak maxima (in minutes). Significant differences between treatments are marked with grey asterisks, and a significant difference between R-GECO1 sensor and CPK21-FRET is indicated with a black asterisk (**$p \leq 0.01$ and * $p \leq 0.05$, respectively; two-way ANOVA and Bonferroni post hoc tests). **I)** Time

(continued)

the mechanistic understanding of response specificity is shifting to the level of Ca^{2+} decoding. Studying isoform-characteristic CDPK-FRET is a promising method for resolving spatiotemporal decoding of Ca^{2+} signatures to uncover the function(s) of CDPKs in signaling pathways of interest.

Materials and Methods

Mutagenesis and cloning of CPK21 and CPK23 enzyme variants

Expression vector *pGEX-6P1* (GE Healthcare)-based recombinant synthesis of *CPK21* and *CPK23* constructs carrying a C-terminal polyhistidine-tag and N-terminal GST-tag was described previously (Geiger et al., 2010). *CPK21* and *CPK23* in *pGEX-6P1* were used as templates for PCR-based site-directed mutagenesis with specific primers to generate the variants CPK21Ile373Ser, CPK21Ile373Asp, CPK23Ser362Ile, and CPK23Ser362Asp (for primer sequences, see Supplemental Table S1) (Weiner et al., 1994). The *CPK23CLD21-Ser362Ile* chimeric construct was generated by replacing a part of the PS of CPK23 (from amino acid [aa] 353), the CLD23 and a part of the *pGEX-6P1* vector backbone in *pGEX-6P1-CPK23* with the homologous sequence from *pGEX-6P1-CPK21* via digestion with HindIII and PstI. To create the *pGEX-6P1-CPK23CLD21* construct, the amino acid substitution Ile362Ser was introduced by site-specific mutagenesis using primers CPK21Ile373Ser-F and CPK21Ile373Ser-R with *CPK23CLD21-Ser362Ile* in *pGEX-6P1* as the PCR template. The *pXCS-CPK23-HA-StrepII in vivo* expression plasmid used in this study has been described (Geiger et al., 2010). Mutations of Asp193 in CPK23 and Asp204 in CPK21 led to kinase-deficient variants (Geiger et al., 2010; Geiger et al., 2011). To create CPK23Asp193Ala, site-directed mutagenesis was conducted using the primers CPK23Asp193Ala-F and CPK23Asp193Ala-R.

Generation of CDPK FRET sensors

Variable and inactive kinase domain coding sequences of *CPK21* and *CPK23* were re-amplified from the plasmids *pXCS-CPK21Asp204Ala-HA-StrepII* (Geiger et al., 2011) and *pXCS-CPK23Asp193Ala-HA-StrepII* using the forward primer CPK21-VK XbaI EcoRI-F or CPK23-VK XbaI EcoRI-F and the reverse primer CPK21/23-VK XbaI-R to introduce flanking XbaI digestion sites. The fragments were digested with XbaI and introduced into pUC-F3-II (Waadt et al., 2014), resulting in *pUC-F3-II-CPK21-VK* (variable and kinase domain) or *pUC-F3-II-CPK23-VK*. *PUC-F3-II* contains the FRET donor (mT) (Goedhart et al., 2010) and the FRET acceptor (Venus circularly permutated at amino acid 173, cpV173) (Nagai

et al., 2004). If not stated otherwise, with 'CPKK' to denote active kinases, kinase-deficient variants were used for all CDPK-FRET fusion proteins. The *CPK21* PS and CLD were isolated by PCR using the primers CPK21-PSCLD ApaI-F and CPK21-PSCLD SmaI-R for linker variant F1, CPK21-PSCLD SpeI-F and CPK21-PSCLD KpnI-R for linker variant F2, or CPK21-PSCLD BamHI-F and CPK21-PSCLD SalI-R for linker variant F3. The PCR products were ligated between the ApaI/SmaI (F1), SpeI/KpnI (F2) and BamHI/SalI (F3) sites of *pUC-F3-II-CPK21-VK*, resulting in *pUC-F3-II-CPK21-FRET* (F1-F3), respectively. The *CPK21* and *CPK23* coding sequences covering the PS and CLD domain until EF-hand 4 (CPK21 aa 522, CPK23 aa 511) were amplified with primers introducing ApaI (CPK21-PSCLD ApaI-F and CPK23-PSCLD ApaI-F) and SmaI (CPK21-PSCLD-EF4 SmaI-R and CPK23-PSCLD-EF4 SmaI-R) restriction sites. The fragments were ligated via ApaI/SmaI into *pUC-F3-II-CPK21-VK* to yield *pUC-F3-II-CPK21-FRET* (F4), or into *pUC-F3-II-CPK23-VK* to yield *pUC-F3-II-CPK23-FRET*. The first 3 base pairs of the SmaI restriction site encode the aa Pro, identical in CPK21 (aa 523) and CPK23 (aa 512). Thus, in *pUC-F3-II-CPK21-FRET* (F4), or in *pUC-F3-II-CPK23-FRET*, CDPK coding sequences up to aa 523 (CPK21) or 512 (CPK23) are present.

E. coli expression vectors were obtained by sub-cloning *CPK21-FRET* (F1-F4) and *CPK23-FRET* via EcoRI/SacI into pET-30a (+) (Novagen). The resulting *pET-30a-CPK21-FRET* (F1-F4) and *pET-30a-CPK23-FRET* constructs carry an N-terminal polyhistidine-tag derived from the *pET-30a* vector backbone and a C-terminal StrepII-tag derived from *pUC-F3-II-CPK21-FRET* (F1-F4) or *pUC-F3-II-CPK23-FRET* constructs. To clone *CPK21*- and *CPK23-FRET* variants, mutation-containing *CDPK* sequences, or the *CPK23CLD21* chimeric sequence, were exchanged via restriction digestion from *pGEX-6P1-CDPK* constructs and ligation into *pET30a-CDPK-FRET* (F4).

The truncated CPK21-FRET variant PS-CLD21 was generated via Golden-Gate cloning using the modular cloning (MoClo) system (Weber et al., 2011). The PS-CLD21 coding sequence was re-amplified from the plasmid *pUC-F3-II-CPK21-FRET* (F4) using the forward primer CPK21-PSCLD-GG-BpiI-F and reverse primer CPK21-PSCLD-GG-BpiI-R, creating a 4 bp sticky overhang that was released upon BpiI treatment and cloned into *pAGM9121*. The mT and cpV173 coding sequences were re-amplified from *pUC-F3-II-CPK21-FRET* (F4) using the primers mT-GG-BpiI-F and mT-GG-BpiI-R for mT and the primers cpV173-GG-BpiI-F and cpV173-StrepII-GG-BpiI-R for cpV173 and cloned into *pAGM9121*. The PS-CLD21, mT and cpV137-StrepII coding sequences were released from the *pAGM9121* vectors

Figure 5. (Continued)
differences in s between R-GECO1 and CPK21-FRET ratio-derived first, second, and third local peak maxima. Significant differences from 0 are marked '*' ($p \leq 0.05$; one sided t-test). 'ns' denotes non-significant differences, and results where $p < 0.1$ are indicated as such. **A–D** and **G–I**, Data are represented by the mean $\pm$ SD (numbers indicate means), where dots represent the individual measurements ($n_{ABA} = 7$, $n_{flg22} = 8$, I, $ABA_{peak2 \text{ and } 3}$ $n = 6$, $flg22_{peak3}$ $n = 7$).

upon BsaI treatment and reassembled in the *E. coli* expression vector *pAGM22082* (Knorrscheidt et al., 2020). The *pAGM22082* vector carries polyhistidine residues adjacent to the BpiI insertion site, allowing the expression of an N-terminal histidine-tag fusion protein. The coding sequences from the mT start codon until the stop codon (mT-PS-CLD21-cpV173-StrepII) are identical between *pAGM 22082-PS-CLD21* and *pET-30a-CPK21*-FRET (F4). *pAGM9121* (Addgene plasmid # 51833; http://n2t.net/addgene:51833; RRID:Addgene_51833) and p*AGM22082* were provided by Sylvestre Marillonnet (Leibniz Institute of Plant Biochemistry, Halle (Saale), Germany).

For *in vivo* transient expression, *CPK21*-FRET and *CPK23*-FRET were sub-cloned via *EcoRI/Ecl136II* and inserted between *EcoRI/SfoI* into *pXCS-HA-StrepII* (Witte et al., 2004), yielding *pXCS-CPK21-* or *pXCS-CPK23*-FRET. The *p35S* of *pXCS-CDPK-FRET* was substituted with the *ubiquitin4-2* promoter from parsley (*Petroselinum crispum*) from *V69-pUbi: Cas9-MCS-U6* (Kirchner et al., 2017) via *AscI/XhoI*, yielding *pXC-Ubi-CPK21*-FRET or *pXC-Ubi-CPK23*-FRET. For cytosolic localization, the *pXC-Ubi-CDPK*-FRET construct was used as a template for PCR-based site-directed mutagenesis, introducing the Gly2Ala-Cys3Val mutation. In the CDPK FRET construct used for the *in vivo* imaging experiments, the FRET donor mT was substituted with eCFP (cyan fluorescent protein) (Supplemental Figure S1B). The primers CFP NdeI-F and CFP ApaI-R were used to amplify *CFP* (Heim and Griesbeck, 2004), introducing *NdeI/ApaI* restriction sites, and *CFP* was cloned into *pXC-Ubi-CPK21Gly2Ala-Cys3Val*-FRET and *pXC-Ubi-CPK23Gly2Ala-Cys3Val*-FRET or, for expression in *E. coli*, into *pET-30a-CPK21*-FRET. In all *in vivo* measurements, CDPK-FRET fusion constructs with eCFP were used.

For estradiol-inducible expression, *CPK21*-FRET was cloned in *pER10*. This estradiol-inducible system for use in transgenic plants has been described elsewhere (Sudarshana et al., 2006). The *CPK21*-FRET coding sequences were re-amplified from *pET-30a-CPK21*-FRET (with eCFP) using the forward primer CPK21 XhoI-F and the reverse primer StrepII. SpeI-R and was cloned into *XhoI SpeI*-linearized *pER10*, yielding *pER10-CPK21*-FRET.

Generation of transgenic plants

Transgenic *A. thaliana* plants were generated by transforming R-GECO1 (Waadt et al., 2017) plants with *pER10-CPK21*-FRET by the floral dip method. Plants were grown under long-day conditions [16 h day light, 20–22°C; 120 µE light intensity provided by a white light (32 W, F32T8/TL841 Philips), 60% RH]. Surface sterilized seeds were sown on 0.5× Murashige and Skoog (MS) media containing 500 mg/L MES and vitamins (Duchefa, Netherlands), 0.8% [w/v] phytoagar (Duchefa), 50 µg/ml kanamycin, pH 5.7 adjusted with KOH. One-week-old kanamycin resistant seedlings were then transferred to 1 mL distilled water containing 10 µM 17-β-estradiol and 0.05% DMSO, incubated for 48 h, and screened for fluorescence using a fluorescence stereo zoom microscope (Zeiss Axio

Zoom.V16, Zeiss) before the transfer to individual pots. Plants were maintained under short-day conditions [8 h day light, 120 µE, provided by a white light (32 W, F32T8/ TL841 Philips), 20–22°C; 60% RH]. All ten selected CPK21-FRET-expressing lines showed a patchy expression pattern or unevenly distributed fluorescence, as reported previously in estradiol inducible systems (Zuo et al., 2000; Schlücking et al., 2013). Two lines with proper 3:1 segregation and fluorescence emission were used for further propagation.

Expression in *E. coli* and protein purification

CDPK constructs were expressed as recombinant double-tagged fusion proteins in *E. coli*. For *in vitro* kinase assays, the expression vector *pGEX-6P1* was used, and proteins were purified using the N-terminal GST-Tag and a C-terminal His-Tag. For *in vitro* FRET measurements, the expression vector *pET30a* or *pAGM22082* was used, and proteins were purified using the N-terminal His-Tag and a C-terminal StrepII-Tag.

To synthesize and purify proteins for the kinase assays, the *pGEX-6P1-CDPK* expression vectors were introduced into *E. coli* BL21 (DE3) (Stratagene). Bacteria were grown at 37°C in LB medium containing 100 µg/ml ampicillin, and protein expression was induced at an OD$_{600}$ of 0.4–0.6 with 0.3 mM Isopropyl-β-d-1-thiogalactopyranoside (IPTG), followed by incubation at 28°C for 4 h. The cells were lysed in 4 ml histidine-lysis buffer (50 mM HEPES-KOH pH 7.4, 300 mM NaCl, 0.2% (v/v) Triton X-100, 1 mM DTT, 10 µl protease inhibitor cocktail for histidine tagged proteins (Sigma)/ 0.2 g of *E. coli* cells and 30 mM imidazole) using 1 mg/ml lysozyme and sonication. After centrifugation, the supernatant was rotated with 300–600 µl Ni Sepharose 6 fast flow (GE Healthcare) at 4°C for 1 h. The sample/Ni Sepharose mixture was loaded onto empty columns and washed 1 × 10 ml histidine-washing buffer (50 mM HEPES-KOH pH 7.4, 300 mM NaCl) with 30 mM imidazole and 1 × 10 ml histidine-washing buffer with 40 mM imidazole. Proteins were eluted 3× in 500 µl histidine-elution buffer (50 mM HEPES-KOH pH 7.4, 300 mM NaCl, 500 mM imidazole). The eluate was incubated at 4°C for 1 h with Glutathione sepharose. The eluate/Glutathione sepharose mixture was loaded onto columns, washed 3 × 3 ml GST-wash buffer (50 mM Tris-HCl pH 8.0, 250 mM NaCl, 1 mM DTT) and eluted 3× with 300 µl GST-elution buffer (100 mM Tris-HCl pH 8.4 and 20 mM glutathione). Proteins were dialyzed using a QuixSep micro dialysis capsule (Roth) and dialysis membrane with 6,000–8,000 Da cut off (Roth). Dialysis-buffer was composed of 30 mM MOPS pH 7.4 and 150 mM KCl.

To synthesize and purify proteins for FRET measurements, *pET30a-CDPK*-FRET expression vectors were transformed into *E. coli* BL21 (DE3) strain pLysS (Stratagene). Bacteria were grown at 37°C in TB medium containing 50 µg/ml kanamycin and 34 µg/ml chloramphenicol, and protein expression was induced at an OD$_{600}$ of 0.4–0.6 with 0.4 mM IPTG, followed by incubation at 22°C for 4 h. Cell lysis and

purification of histidine tagged proteins were performed as described for GST-CDPK-His fusion proteins (see above). The His-eluate was incubated at 4°C for 45 min with Strep-tactin macroprep (IBA). StrepII-tagged recombinant proteins were purified as described by Schmidt and Skerra (Schmidt and Skerra, 2007) with the modification that EDTA was omitted from the elution and wash buffer. Proteins were dialyzed using a QuixSep micro dialysis capsule (Roth) and dialysis membrane with 6,000–8,000 Da cut-off (Roth). Dialysis buffer was composed 30 mM Tris-HCl pH 7.4, 150 mM NaCl and 10 mM MgCl$_2$. 10% SDS-PAGE and Coomassie staining confirmed the purity of *E. coli* expressed proteins. For *in vitro* analyses, protein concentrations were quantified based on the Bradford method (Protein assay, Bio-Rad).

Protein sequence comparison

The analysis of the PS of the entire *A. thaliana* Col-0 CDPK gene family was conducted using amino acid sequences acquired from UniProt (UniProt Consortium, 2021) with the program Web Logo (Schneider and Stephens, 1990; Crooks et al., 2004).

Preparation of Ca^{2+} and Mg^{2+} buffers

For CDPK protein kinase assays, reciprocal dilutions of zero-Ca^{2+}-buffer (10 mM EGTA 150 mM KCl, 30 mM MOPS pH 7.4) with high-Ca^{2+}-buffer (10 mM CaCl$_2$, 10 mM EGTA 150 mM KCl, 30 mM MOPS pH 7.4) were mixed. For the analysis of CDPK-FRET conformational changes, high-Ca^{2+}-buffer (20 mM CaCl$_2$; 20 mM EGTA, 150 mM NaCl, 10 mM MgCl$_2$, 30 mM Tris-HCl pH 7.4) and zero-Ca^{2+}-buffer (20 mM EGTA, 150 mM NaCl, 10 mM MgCl$_2$, 30 mM Tris-HCl pH 7.4) were mixed accordingly and combined with the CDPK-FRET fusion proteins at 1:1 dilution. Correspondingly, buffer solutions for CDPK-FRET analysis in a Mg^{2+} concentration gradient were prepared by mixing high-Mg^{2+}-buffer (120 mM MgCl$_2$, 20 mM EDTA, 150 mM NaCl, 30 mM Tris-HCl pH 7.4) and zero-Mg^{2+}-buffer (20 mM EDTA, 150 mM NaCl, 30 mM Tris-HCl pH 7.4), followed by a 1:1 dilution with CDPK-FRET protein in Mg^{2+}-dialysis buffer (30 mM Tris-HCl pH 7.4, 150 mM NaCl) before data acquisition. The indicated free Ca^{2+}- or Mg^{2+}-concentrations were calculated on the WEBMXC extended website http://tinyurl.com/y48t33xq based on (Patton et al., 2004).

In vitro kinase assays

In vitro kinase activity assays with recombinant purified proteins were conducted as described (Franz et al., 2011), using a 20 aa peptide (41-RGPNRGKQRPFRGFSRQVSL-60; JPT Peptide Technologies) derived from the CPK21 and CPK23 *in vivo* phosphorylation substrate protein SLAC1 (SLOW ANION CHANNEL-ASSOCIATED 1). For kinase reactions (30 µl), the enzyme (∼ 90 nM) was incubated in 25 mM MOPS pH 7.4, 125 mM KCl, 10 mM MgCl$_2$, 10 µM ATP, 3 µCi [γ-^{32}P]-ATP, 10 µM SLAC1 peptide, 6.67 mM EGTA

and different concentration of CaCl$_2$. Purified enzyme was added to 2–4 premixed reaction mixtures resulting in 2–4 technical replicates and incubated for 20 min at 22°C. The reaction was stopped by adding 3 µl 10% phosphoric acid. Phosphorylation of the SLAC1 peptide was assessed after the binding of phosphor-peptides to P81 filter paper and scintillation counting as described (Franz et al., 2011). Ca^{2+}-dependent kinase activity was analyzed by a four-parameter logistic equation and indicated as the percentage of maximal activity. To analyze the autophosphorylation activities of protein kinases, the reaction was the same as above except that SLAC1 substrate peptide was omitted from the kinase reaction and ∼255 nM enzyme was used. The reaction was stopped by adding 5 × SDS-PAGE loading buffer and boiling for 5 min, and the samples were separated by 10% SDS-PAGE. Phosphorylation was determined by autoradiography and phospho-imaging (Typhoon FLA 9500, GE Healthcare).

In vitro analyses of CDPK-FRET

CDPK-FRET protein (∼415 nM) in dialysis buffer diluted 1:1 with Ca^{2+}-buffers of defined concentrations was evaluated using a TECAN Infinite M200 PRO plate reader (TECAN) or a SPARK R multimode plate reader (TECAN). Excitation at 435 nm (bandwidth 5 nm) and emission within the range of 470–600 nm were monitored in 2 nm steps with 10 flashes of 20 µs and 400 Hz. CpVenus173/mT emission ratios were calculated based on maximal values from emission bands of mT (470–490 nm) and cpVenus173 (518–538 nm). Emission ratios were plotted against increasing Ca^{2+}-concentrations using a four-parameter logistic equation. A four parameter logistic equation can be written as an equation that defines the response (here cpVenus173/mT emission ratios) as a function of dose (here Ca^{2+}-concentration) and four parameters: Y = Bottom + (Top-Bottom)/(1 + 10^(LogEC50-X)*Hill slope) (Motulsky and Christopoulos, 2004). The best fit-value obtained for bottom (base level) of cpVenus173/mT emission ratio is used to calculate Δ R as the percentage change of emission ratios. Δ R is defined as:

$$\Delta R[_{free}Ca^{2+}]_{x\,\mu M} = \frac{R\ [Ca^{2+}]_{x\,\mu M}}{R\ Bottom} \times 100 - 100$$

The percentage change of emission ratio is fitted by a four-parameter logistic equation.

The pH-dependency of a CDPK-FRET sensor was assessed with CPK21-FRET in dialysis buffers (30 mM Tris-HCl, 150 mM NaCl and 10 mM MgCl$_2$) of different pH values (pH 5.0, 6.9, and 8.0). Dialyzed proteins were diluted 1:1 with either high-Ca^{2+}-buffer or zero-Ca^{2+}-buffer (see above) in 30 mM Tris-HCl adjusted accordingly to a pH range between 5.0 and 8.4.

Protein expression in Arabidopsis protoplasts and purification for MS measurement

Preparation and transfection of ∼ 2.4 × 10^5 Arabidopsis leaf mesophyll protoplasts from *cpk23* (SALK_007958) (Ma and

Wu, 2007) for transient expression of CPK23-HA-StrepII and kinase inactive CPK23D193A-HA-StrepII was conducted as described (Wu et al., 2009). Following incubation for 14 h, half of the protoplast sample was treated with 30 µM ABA for 10 min at room temperature. Cells were collected by two repeated centrifugation steps. After the centrifuge had accelerated to 10,000 × *g*, the centrifugation was continued for 2 s. Harvested protoplasts were frozen in liquid nitrogen. The protoplasts were resuspended in 600 µl of extraction buffer [100 mM Tris-HCl pH 8.0, 100 mM NaCl, 5 mM EDTA, 5 mM EGTA, 20 mM DTT, 10 mM NaF, 10 mM NaVO₄, 10 mM β-glycerol-phosphate, 0.5 mM AEBSF, 2 µg/ml aprotinin, 2 µg/ml leupeptin, 100 µg/ml avidin, 0.2% NP-40, 1× phosphatase inhibitor mixture (Merck) and 1× protease inhibitor mixture (Merck)] and centrifuged at 20,000 × *g* for 10 min at 4°C. The supernatant was incubated with 24 µl Strep-Tactin MacroPrep (IBA) beads for 45 min at 4°C. After centrifugation (500 × *g*, 1 min), the beads were dissolved in 100 µl 6 M urea, 2 M thiourea, pH 8.0 and incubated for 10 min at 4°C. After another centrifugation step (500 × *g*, 1 min), the protein-containing supernatant was transferred to a new tube, and the reduction of disulfide bonds, alkylation of cysteines and tryptic digestion were conducted as described (Dubiella et al., 2013). Peptide-containing reactions were vacuum-dried at 30°C and stored at −20°C.

Targeted analysis of phosphorylation by directed MS of the *in planta* phosphorylation assay

The samples were subsequently desalted through C18 tips. C18 tips were hand made from C18 disks (Empore C18 Extraction Disk, Sigma Aldrich) as described in (Rappsilber et al., 2003). Digested protein mixtures were spiked with 500 fmol of 13C₆-R/K mass-labelled standard peptide before mass spectrometry analysis. Tryptic peptide mixtures including the stable-isotope labelled standard peptides were analyzed on a nano-HPLC (Easy nLC, Thermo Scientific) coupled to an Orbitrap mass spectrometer (LTQ-Orbitrap, Thermo Scientific) as the mass analyzer. Peptides were eluted from a 75 µm analytical column (Easy Columns, Thermo Scientific) on a linear gradient running from 10% to 30% acetonitrile over 120 min and were ionized by electrospray. The target peptide V(pS)AVSLSEEEIK (m/z of doubly-charged ion for phosphopeptide 685.8262; non-phosphopeptide 645.8430) was analyzed in its phosphorylated and non-phosphorylated states using the stable-isotope labelled synthetic standard peptide as an internal reference and for normalization between samples. Standards carried a ¹³C₆-labeled amino acid (arginine or lysine) at their C-terminal ends. Information-dependent acquisition of fragmentation spectra for multiple-charged peptides was used with preferred precursor selection of the target peptides through implementation of an inclusion lists (Schmidt et al., 2011). Full scans were obtained at a resolution of full width at half maximum of 60,000, CID fragment spectra were acquired in the LTQ. Additional fragmentation though

multistage activation (Schroeder et al., 2004) was used if the peptides displayed a loss of phosphoric acid (neutral loss, 98 Da) upon MS/MS fragmentation. Protein identification and intensity quantitation were performed as described (Menz et al., 2016). To allow robust identification and quantitation of the internal standard peptide, multiplicity was set to 2 and Lys6 and Arg6 were selected as stable isotope labels and, in general, data analysis was focused on the target peptide sequences only.

Quantification of changes in target peptide abundance (*in planta* phosphorylation assay)

For quantitative analysis, the ion intensities of ¹³C₆-labeled standard peptides were used for normalization between samples and replicates. Normalized ion intensities of phosphorylated and non-phosphorylated target peptides were averaged between replicates of the same treatments.

In vitro auto-phosphorylation assays for mass spectrometry analysis

For kinase reactions, (150 µl) recombinant purified proteins (∼ 3.75 µM) were incubated in 25 mM MOPS, pH 7.4, 125 mM KCl, 10 mM MgCl₂, 10 µM ATP, and 6.67 mM EGTA with and without 6.67 mM CaCl₂ for 20 min at 22°C. The reaction was stopped by adding 5× SDS-PAGE loading buffer and boiling for 10 min. Samples were split into technical replicates and separated by 10% SDS-PAGE.

Phosphoproteomic analysis for the *in vitro* auto-phosphorylation assay

For targeted MS-analysis (parallel reaction monitoring, PRM) of *E. coli* samples, dried peptides were dissolved in 5% acetonitrile, 0.1% trifluoric acid and injected into an EASY-nLC 1200 liquid chromatography system (Thermo Fisher Scientific). Peptides were separated using liquid chromatography C18 reverse phase chemistry employing a 120 min gradient increasing from 1% to 32% acetonitrile in 0.1% FA, and a flow rate of 250 nL/min. The eluted peptides were electrosprayed on-line into a Fusion Lumos Tribrid mass spectrometer (Thermo Fisher Scientific) with a spray voltage of 2.0 kV and a capillary temperature of 305°C. A full MS survey scan was carried out with chromatographic peak width set to 30 s, resolution 60,000, automatic gain control (AGC) set to standard and a max injection time (IT) of 100 ms. MS/MS peptide sequencing was performed using a PRM scan strategy (without retention time scheduling), with HCD fragmentation containing target peptide m/z on a list (Supplemental Table S2). MS/MS scans were acquired in the Orbitrap with Loop control set to all and resolution to 15,000, mass to charge ratios (m/z) between 300 and 2,000, AGC target set to 300%, Maximum IT 120 ms, isolation width 2.0 m/z, and normalized collision energy 28%.

Peptide and protein identification was conducted with MaxQuant v2.0.1.0 (Cox and Mann 2008). Mass spectra were annotated against the *E. coli* proteome (UniProt Taxonomy ID 83333) adjusted with amino acid sequences of CPK23 protein

variants. Phosphopeptide identification information was extracted from the MaxQuant evidence file (Supplemental Table S3). Methionine oxidation and protein N-terminal acetylation, serine, threonine and tyrosine phosphorylation were set as variable modifications, while carbamidomethylation of cysteine was set as the fixed modification. For label-free quantitation, Fast LFQ and retention time matching between runs was chosen. For PRM quantification analyses with Skyline (version 20.2.0.343), a spectral library was generated using the MaxQuant msms.txt search results, applying a cut-off score of 0.95. Ambiguous peptide matches were excluded, and the library was filtered for peptides spanning the S362 phosphosite. *.raw files were imported into Skyline and automated fragment ion selection by Skyline was utilized (6 ions/peptide): MS/MS ion trace filtering (centroid mode) and charge states of $1+/2+/3+$ for b- and y-ions as well as $2+/3+$ for precursor ions. Integration boundaries of peptides were inspected manually and corrected, if necessary. Peptides with truncated peaks or no MS/MS signal were excluded from further analysis. Reports were exported and further processed in MS Excel. For peptide quantification, the summed AUC of fragment ions was used, and the relative abundances of all pS362 peptides compared to all peptides spanning the modification site were calculated.

Transient pollen transformation

N. tabacum (cultivar Petit Havana SR1) plants were grown in soil with a day/night regime of 10 h/14 h and a temperature of 22 to 24/20 to 22°C provided by a 30 klx white light (SON-T Agro 400W; Philips). Pollen of tobacco lines expressing the R-GECO1 Ca^{2+} sensor (Zhao et al., 2011) as a stable transgene under the control of a pollen specific promoter (*pLeLAT52:R-GECO1* line) was used from frozen stocks to perform transient transformation using a homemade particle bombardment device that was previously described in detail (Gutermuth et al., 2013). Biolistic transformation was performed with *pXC-Ubi-CPK21Gly2Ala-Cys3Val-CFP* and *pXC-Ubi-CPK23Gly2Ala-Cys3Val-CFP* on agar plates containing pollen tube growth medium containing 10 mM Cl^- (1 mM MES-Tris pH 5.8, 0.2 mM $CaCl_2$, 9.6 mM HCl, and 1.6 mM H_3BO_3). 10 mM Cl^- were used to provoke tip-focused dynamic Ca^{2+}-oscillation patterns. The osmolality of the pollen medium was adjusted to 400 mosmol kg^{-1} (Vapor Pressure Osmometer 5520) with D(+)-sucrose.

Live-cell fluorescence imaging in pollen tubes

The setup for wide-field live-cell imaging and the appropriate software to control sample acquisition have been described in detail (Gutermuth et al., 2013). Images were recorded with a time interval of 5 s. For simultaneous CFP/YFP/RFP-imaging, a triple-band dichroic mirror (Chroma # 69008; ET—ECFP/EYFP/mCherry) was used to reflect excitation light on the samples. Excitation of CFP and R-GECO1 was performed with a VisiChrome High-Speed Polychromator System (Visitron Systems) at 420 nm and 550 nm, respectively. Optical filters (Chroma Technology Corporation) for CFP (ET 470/24 nm), YFP (ET 535/30 nm),

and R-GECO1 (624/40) were used for fluorescence detection with a back-illuminated 512×512 pixel Evolve EMCCD camera (Photometrics). A high-speed 6-position filter wheel (Ludl Electronic Products Ltd.) ensured the quasi simultaneous imaging of all three channels with a lag-time of ~ 0.1 s. For image processing, the following steps were conducted for R-GECO1 (R-GECO1 $_{excitation}$/R-GECO1 $_{emission}$), FRET (CFP $_{excitation}$/YFP $_{emission}$) and CFP (CFP $_{excitation}$/CFP $_{emission}$) channels using Fiji (National Institute of Health) (Schindelin et al., 2012) background subtraction (same value for FRET and CFP channel), Gaussian blur, 32-bit conversion, kymograph generation, and threshold adjustment. A self-made script for Octave 4.0.3 free software (http://www.gnu.org/software/octave/) was used to quantify fluorescence intensities of each channel at ~ 5–15 μm behind the tip of the growing pollen tubes over time, as described in (Gutermuth et al., 2018). FRET-analysis was performed by dividing the CFP $_{excitation}$/YFP $_{emission}$ signal by the CFP signal. For optical representation (CDPK-FRET kymographs and example pollen tubes images), ratio images were calculated by dividing the CFP $_{excitation}$/YFP $_{emission}$ by CFP signal using Fiji. Synchronization analyses were performed with R v.4.1 (R Core Team, 2022) as described for live-cell fluorescence imaging in guard cells (Li et al., 2021).

Live-cell fluorescence imaging in guard cells

To prepare epidermal peel samples, leaf material from 2 to 3 week old plants grown in jiffy-7 soil (Jiffy Products) under short-day conditions [10 h day light, 20–22°C; 120 μE light intensity provided by a white light (32 W, F32T8/TL841 Philips), 60% RH] were used. Epidermal peel sample preparation in 2 well chambered coverslips (IBIDI) has been described in detail (Eichstädt et al., 2021). The peels were directly immersed in 1 ml plant buffer (10 mM MES-Tris pH 6.15, 5 mM KCl, 50 μM $CaCl_2$, 20 μM 17-β-estradiol and 0.05% DMSO), and the samples were incubated for recovery overnight. The samples were incubated in the light at 20–22°C for at least 2 h before imaging. Confocal imaging was performed in bottom imaging mode on a Zeiss LSM 880 system (Zeiss) with a $40 \times$ water immersion objective (LD C-APOCHROME, 40×/1.1 Korr UV-VIS M27; Zeiss). 16-bit images were acquired every 4.16 s with a frame size of 512×512 pixels and a pinhole of 599 μm. Fluorescent proteins were excited with 458 (eCFP $_{excitation}$/eCFP $_{emission}$ and eCFP $_{excitation}$/YFP $_{emission}$), 514 (YFP $_{excitation}$/YFP $_{emission}$) and 561 (R-GECO1 $_{excitation}$/R-GECO1 $_{emission}$) nm, and an emission-range between 465 and 505 nm for eCFP, 525 and 560 nm for YFP or 580 and 611 nm for R-GECO1 was used for detection. Guard cells showing a constant resting Ca^{2+} level were selected to analyze Ca^{2+} increase upon stimulus application. The nature and function of spontaneous Ca^{2+} transients occurring in some guard cells were discussed elsewhere (Allen et al., 1999; Klüsener et al., 2002; Hubbard et al., 2012).

For 100 nM flg22 and 20 μM ABA treatments, 50-fold concentrations were prepared in water (flg22) or 10% ethanol (ABA) and added at a 1:50 volume ratio. Treatment with

ethanol (0.2% final) as the solvent control did not induce measurable signal increases of R-GECO1 or CPK21-FRET (Supplemental Figure S10). For image processing, the following steps were conducted for R-GECO1 (R-GECO1 $_{excitation}$/R-GECO1 $_{emission}$), FRET (CFP $_{excitation}$/YFP $_{emission}$) and CFP (CFP $_{excitation}$/CFP $_{emission}$) channels using Fiji: Gaussian blur filter set to 1, 32-bit conversion and threshold adjustment (stack histogram). For optical representation (CDPK conformation sensor example guard cell images), ratio images were calculated by dividing the CFP $_{excitation}$/YFP $_{emission}$ by CFP signal using Fiji. For quantification, single entire guard cells were selected as ROIs. The mean grey values of these ROIs were used for further calculations. The FRET ratio was calculated by dividing FRET (CFP $_{excitation}$/YFP $_{emission}$) mean grey values over CFP (CFP $_{excitation}$/CFP $_{emission}$) mean grey values. The resulting FRET emission ratio and the R-GECO1 signal was normalized to the mean of the 10 frames before treatment (R/R_0) or (F/F_0). For graphic representation intensity-over-time plots, data were plotted and smoothed (averaging 15 values on each side using a second order polynomial) with GraphPad Prism 5 software. Before synchronization analysis of stomatal measurements, the normalized FRET emission ratio and normalized R-GECO1 fluorescence were adjusted to signal changes derived from technical artefacts (such as stomatal movement) by calculating a trend line. The following steps were performed in R v. 4.1 with R studio (R Core Team, 2022; Team, 2022) using the R packages *scales* (Wickham et al., 2022a), *readxl* (Wickham et al., 2022b), *writexl* (Ooms, 2021) *stats* and *forecast* (Hyndman and Khandakar, 2008; Hyndman et al., 2022). To calculate this trend line, a linear regression model was applied with time as the predictor variable and signal (normalized FRET emission ratio and normalized R-GECO1 fluorescence) as the response variable, assuming that the technical artefacts can be represented by a linear relationship. The values of the linear regression model were used to revise the data by dividing the normalized signals by the corresponding data of the linear regression. Synchronization analysis for Ca²⁺ and CDPK-FRET conformational change were used to quantify their phase relationship by cross correlation analysis with an R-script called phase_analysis, which was described previously (Li et al., 2021). To analyze the signal change dynamics (AUC), the following steps were conducted in R v. 4.1: the revised data were smoothed by a moving average (8 data points; centered) and rescaled between 0 (minimum of the signals) and 1 (maximum of the signals) for the time points after treatment. The AUC data were calculated using GraphPad Prism 5.

Statistical analysis
Analyses of kinase activities and conformational changes were performed using a four-parameter logistic equation with a global model with shared Hill slope for all data sets of the same enzyme using GraphPad Prism 5. To compare enzyme variants, data from different measurements were combined in one figure. Statistical analyses of variance (*t*-test, ANOVA) were performed using GraphPad Prism 5 (Supplemental Data Set S1).

Accession numbers
Sequence data for all genes examined in this study can be found in the GenBank/EMBL libraries (https://www.ncbi.nlm.nih.gov/) or the Arabidopsis Information Resource (https://www.arabidopsis.org) under the following accession numbers: CPK21 (AT4G04720) and CPK23 (AT4G04740). Accession number based on the RCSB protein data bank (https://www.rcsb.org) of *Toxoplasma gondii* CDPK1 3D structures are for the active structure (3HX4) and for the inactive structure (3KU2). Protein sequence data for the 34 AtCDPKs can be found in UniProt (https://www.uniprot.org/) under the following accession numbers: CPK1 A0A178UQJ5, CPK2 A0A178VDL8, CPK3 A0A178V4I3, CPK4 A0A178UX60, CPK5 A0A178V3J8, CPK6 Q38872, CPK7 A0A178UIX, CPK8 A0A654G2M0, CPK9 A0A178V5W2, CPK10 A0A654EC48, CPK11 Q39016, CPK12 Q42396, CPK13 A0A178VEY4, CPK14 A0A178VYK9, CPK15 F4JKC7, CPK16 Q7XJR9, CPK17 A0A178URQ6, CPK18 F4JNY4, CPK19 Q1PFH8, CPK20 A0A178VWI7, CPK21 A0A178USG2, CPK22 A0A1P8B715, CPK23 F4JGW8, CPK24 A0A178VS64, CPK25 A0A178VQ54, CPK26 F4JTL3, CPK27 Q9ZSA4, CPK28 A0A178UH42, CPK29 Q8RWL2, CPK30 A0A178W4G7, CPK31 Q9S9V0, CPK32 A0A178VB71, CPK33 A0A1P8ANC2, CPK34 Q3E9C0.

Author contributions
A.L. conceived the study and established conformational change analysis using CDPK-FRET, performed all *in vitro* kinase assays and conducted *in vivo* imaging. B.E. performed the cloning of FRET-constructs and *in vitro* conformational change analyses. S.L. wrote R-scripts, performed analyses and *in vitro* conformational change analyses for PS-CLD21; P.S. conducted protein expression and preparation for MS

analysis of the *in planta* phosphorylation assay. J.O. conducted expression analyses of the pEstradiol CPK21-FRET line. S.M performed MS analysis of the *in vitro* auto-phosphorylation assay and evaluation. W.X.S. performed MS analysis of the *in planta* phosphorylation assay and evaluation. K.R.K. designed and supervised the *in vivo* imaging experiments in pollen tubes and generated the tobacco line used. J.A.F. participated in strategic discussions and contributed to experimental design. T.R. conceived the study and contributed to the experimental design. A.L. and T.R. wrote the manuscript. All authors discussed the results and commented on the manuscript.

Supplemental data

The following materials are available in the online version of this article.

Supplemental Figure S1: Design and *in vitro* characterization of the CDPK-FRET reporter.

Supplemental Figure S2: *In vitro* kinase activity measurements of the CPK21-FRET conformational change sensor.

Supplemental Figure S3: EC50 and K50 values document isoform- and mutated variant-specific Ca^{2+}-responsiveness of kinase activity and conformational changes.

Supplemental Figure S4: Influence of CPK23 auto-phosphorylation on Ca^{2+}-responsiveness.

Supplemental Figure S5: CPK23 undergoes auto-phosphorylation at Ser362.

Supplemental Figure S6: Tip-focused intracellular Ca^{2+} gradients and conformational change of CPK21 upon transient expression of CPK21Gly2Ala-Cys3Val FRET fusion protein in tobacco pollen tubes.

Supplemental Figure S7: CPK23 is unable to decode the tip-focused intracellular Ca^{2+} gradient and Ca^{2+}-oscillations in growing tobacco pollen tubes.

Supplemental Figure S8: ABA dependent Ca^{2+}-concentration transients in Arabidopsis guard cells are decoded by CPK21.

Supplemental Figure S9: CPK21-FRET decodes flg22-induced cytosolic Ca^{2+}-concentration transients in Arabidopsis guard cells.

Supplemental Figure S10: Flg22 but not the solvent control EtOH induces cytosolic Ca^{2+}-concentration transients and CPK21 conformational changes.

Supplemental Figure S11 Synchronization analysis between CPK21-FRET and R-GECO1 in the pollen tube tip.

Supplemental Table S1: Sequences of oligonucleotide primers.

Supplemental Table S2: PRM inclusion list (Fusion Lumos Tribrid MS).

Supplemental Table S3: Phosphopeptide identification information extracted from the MaxQuant evidence file.

Supplemental Data Set S1: Statistical analysis of ANOVA and *t*-test results for the data shown in the figures.

References

Allen GJ, Kwak JM, Chu SP, Llopis J, Tsien RY, Harper JF, Schroeder JI. Cameleon calcium indicator reports cytoplasmic calcium dynamics in Arabidopsis guard cells. The Plant Journal. 1999:**19**(6):735–747. doi:10.1046/j.1365-313x.1999.00574.x

Bender KW, Blackburn RK, Monaghan J, Derbyshire P, Menke FL, Zipfel C, Goshe MB, Zielinski RE, Huber SC. Autophosphorylation-based calcium (Ca^{2+}) sensitivity priming and Ca^{2+}/Calmodulin inhibition of *Arabidopsis thaliana* Ca^{2+}-dependent protein kinase 28 (CPK28). The Journal of Biological Chemistry. 2017:**292**(10):3988–4002. doi:10.1074/jbc.M116.763243

Bender KW, Zielinski RE, Huber SC. Revisiting paradigms of Ca^{2+} signaling protein kinase regulation in plants. The Biochem Journal. 2018:**475**(1):207–223. doi:10.1042/BCJ20170022

Bernstein, H.J. RasMol. http://www.rasmol.org/. 2009

Bi G, Su M, Li N, Liang Y, Dang S, Xu J, Hu M, Wang J, Zou M, Deng Y, et al. The ZAR1 resistosome is a calcium-permeable channel triggering plant immune signaling. Cell. 2021:**184**(13):3528–3541.e12. doi:10.1016/j.cell.2021.05.003

Billker O, Lourido S, Sibley LD. Calcium-dependent signaling and kinases in apicomplexan parasites. Cell Host & Microbe. 2009:**5**(6):612–622. doi:10.1016/j.chom.2009.05.017

Bjornson M, Pimprikar P, Nürnberger T, Zipfel C. The transcriptional landscape of *Arabidopsis thaliana* pattern-triggered immunity. Nature Plants. 2021:**7**(5):579–586. doi:10.1038/s41477-021-00874-5

Boudsocq M, Droillard MJ, Regad L, Laurière C. Characterization of Arabidopsis calcium-dependent protein kinases: activated or not by calcium? The Biochemical Journal. 2012:**447**(2):291–299. doi:10.1042/BJ20112072

Boudsocq M, Willmann MR, McCormack M, Lee H, Shan L, He P, Bush J, Cheng SH, Sheen J. Differential innate immune signalling via Ca^{2+} sensor protein kinases. Nature. 2010:**464**(7287):418–422. doi:10.1038/nature08794

Brandt B, Munemasa S, Wang C, Nguyen D, Yong T, Yang PG, Poretsky E, Belknap TF, Waadt R, Alemán F, et al. Calcium specificity signaling mechanisms in abscisic acid signal transduction in Arabidopsis guard cells. eLife. 2015:**4**:e03599. doi:10.7554/eLife.03599

Bredow M, Bender KW, Johnson Dingee A, Holmes DR, Thomson A, Ciren D, Tanney CAS, Dunning KE, Trujillo M, Huber SC, et al. Phosphorylation-dependent subfunctionalization of the calcium-dependent protein kinase CPK28. Proceedings of the National Academy of Sciences of the United States of America. 2021:**118**(19):e2024272118. doi:10.1073/pnas.2024272118

Brumbaugh J, Schleifenbaum A, Gasch A, Sattler M, Schultz C. A dual parameter FRET probe for measuring PKC and PKA activity in living cells. Journal of the American Chemical Society. 2006:**128**(1):24–25. doi:10.1021/ja0562200

Chandran V, Stollar EJ, Lindorff-Larsen K, Harper JF, Chazin WJ, Dobson CM, Luisi BF, Christodoulou J. Structure of the regulatory apparatus of a calcium-dependent protein kinase (CDPK): A novel mode of calmodulin-target recognition. J Mol Biol. 2006:**357**(2):400–410. doi:10.1016/j.jmb.2005.11.093

Cox, J., and Mann, M. MaxQuant enables high peptide identification rates, individualized p.p.b.-range mass accuracies and proteome-wide protein quantification. Nature Biotechnology. 2008;**26**:1367–1372. doi:10.1038/nbt.1511

Crooks GE, Hon G, Chandonia JM, Brenner SE. WebLogo: A sequence logo generator. Genome research. 2004:**14**(6):1188–1190. doi:10.1101/gr.849004

Damineli DSC, Portes MT, Feijó JA. Oscillatory signatures underlie growth regimes in Arabidopsis pollen tubes: computational methods to estimate tip location, periodicity, and synchronization in growing cells. Journal of experimental botany. 2017:**68**(12):3267–3281. doi:10.1093/jxb/erx032

Demir F, Horntrich C, Blachutzik JO, Scherzer S, Reinders Y, Kierszniowska S, Schulze WX, Harms GS, Hedrich R, Geiger D, et al. Arabidopsis nanodomain-delimited ABA signaling pathway regulates the anion channel SLAH3. Proceedings of the National Academy of Sciences of the United States of America. 2013:**110**(20):8296–8301. doi:10.1073/pnas.1211667110

Depry C, Zhang J. Using FRET-based reporters to visualize subcellular dynamics of protein kinase A activity. Methods in molecular biology. 2011:**756**:285–294. doi:10.1007/978-1-61779-160-4_16

Dubiella U, Seybold H, Durian G, Komander E, Lassig R, Witte CP, Schulze WX, Romeis T. Calcium-dependent protein kinase/NADPH oxidase activation circuit is required for rapid defense signal propagation. Proceedings of the National Academy of Sciences of the United States of America. 2013:**110**(21):8744–8749. doi:10.1073/pnas.1221294110

Durian G, Sedaghatmehr M, Matallana-Ramirez LP, Schilling SM, Schaepe S, Guerra T, Herde M, Witte CP, Mueller-Roeber B, Schulze WX, et al. Calcium-dependent protein kinase CPK1 controls cell death by *in vivo* phosphorylation of senescence master regulator ORE1. The Plant cell. 2020:**32**(5):1610–1625. doi:10.1105/tpc.19.00810

Eichstädt B, Lederer S, Trempel F, Jiang X, Guerra T, Waadt R, Lee J, Liese A, Romeis T. Plant immune memory in systemic tissue does not involve changes in rapid calcium signaling. Frontiers in plant science. 2021:**12**:798230. doi:10.3389/fpls.2021.798230

Felle HH. pH: Signal and messenger in plant cells. Plant Biology. 2001:**3**(6):577–591. doi:10.1055/s-2001-19372

Franz S, Ehlert B, Liese A, Kurth J, Cazalé A-C, Romeis T. Calcium-dependent protein kinase CPK21 functions in abiotic stress response in *Arabidopsis thaliana*. Molecular plant. 2011:**4**(1):83–96. doi:10.1093/mp/ssq064

Fu D, Zhang Z, Wallrad L, Wang Z, Höller S, Ju C, Schmitz-Thom I, Huang P, Wang L, Peiter E, et al. Ca²⁺-dependent phosphorylation of NRAMP1 by CPK21 and CPK23 facilitates manganese uptake and homeostasis in Arabidopsis. Proceedings of the National Academy of Sciences of the United States of America. 2022:**119**(40):e2204574119. doi:10.1073/pnas.2204574119

Geiger D, Maierhofer T, Al-Rasheid KAS, Scherzer S, Mumm P, Liese A, Ache P, Wellmann C, Marten I, Grill E, et al. Stomatal closure by fast abscisic acid signaling is mediated by the guard cell anion channel SLAH3 and the receptor RCAR1. Science signaling. 2011:**4**(173):ra32. doi:10.1126/scisignal.2001346

Geiger D, Scherzer S, Mumm P, Marten I, Ache P, Matschi S, Liese A, Wellmann C, Al-Rasheid KAS, Grill E, et al. Guard cell anion channel SLAC1 is regulated by CDPK protein kinases with distinct Ca²⁺ affinities. Proceedings of the National Academy of Sciences of the United States of America. 2010:**107**(17):8023–8028. doi:10.1073/pnas.0912030107

Gifford JL, Walsh MP, Vogel HJ. Structures and metal-ion-binding properties of the Ca²⁺-binding helix–loop–helix EF-hand motifs. The Biochemical Journal. 2007:**405**(2):199–221. doi:10.1042/BJ20070255

Goedhart J, van Weeren L, Hink MA, Vischer NO, Jalink K, Gadella TW Jr. Bright cyan fluorescent protein variants identified by fluorescence lifetime screening. Nature Methods. 2010:**7**(2):137–139. doi:10.1038/nmeth.1415

Guo J, He J, Dehesh K, Cui X, Yang Z. CamelliA-based simultaneous imaging of Ca²⁺ dynamics in subcellular compartments. Plant Physiology. 2022:**188**(4):2253–2271. doi:10.1093/plphys/kiac020

Gutermuth T, Herbell S, Lassig R, Brosché M, Romeis T, Feijó JA, Hedrich R, Konrad KR. Tip-localized Ca²⁺-permeable channels control pollen tube growth via kinase-dependent R- and S-type anion channel regulation. The New Phytologist. 2018:**218**(3):1089–1105. doi:10.1111/nph.15067

Gutermuth T, Lassig R, Portes MT, Maierhofer T, Romeis T, Borst JW, Hedrich R, Feijó JA, Konrad KR. Pollen tube growth regulation by free anions depends on the interaction between the anion channel SLAH3 and calcium-dependent protein kinases CPK2 and CPK20. The Plant cell. 2013:**25**(11):4525–4543. doi:10.1105/tpc.113.118463

Guzel Deger A, Scherzer S, Nuhkat M, Kedzierska J, Kollist H, Brosché M, Unyayar S, Boudsocq M, Hedrich R, Roelfsema MR. Guard cell SLAC1-type anion channels mediate flagellin-induced stomatal closure. The New Phytologist. 2015:**208**(1):162–173. doi:10.1111/nph.13435

Harmon AC, Gribskov M, Harper JF. CDPKs—a kinase for every Ca²⁺ signal? Trends in Plant Science. 2000:**5**(4):154–159. doi:10.1016/S1360-1385(00)01577-6

Heim N, Griesbeck O. Genetically encoded indicators of cellular calcium dynamics based on troponin C and green fluorescent protein. The Journal of Biological Chemistry. 2004:**279**(14):14280–14286. doi:10.1074/jbc.M312751200

Huang J-Z, Hardin SC, Huber SC. Identification of a novel phosphorylation motif for CDPKs: Phosphorylation of synthetic peptides lacking basic residues at P-3/P-4. Arch. Biochem. Biophys. 2001:**393**(1):61–66. doi:10.1006/abbi.2001.2476

Huang S, Waadt R, Nuhkat M, Kollist H, Hedrich R, Roelfsema MRG. Calcium signals in guard cells enhance the efficiency by which abscisic acid triggers stomatal closure. The New Phytologist. 2019:**224**(1):177–187. doi:10.1111/nph.15985

Hubbard KE, Siegel RS, Valerio G, Brandt B, Schroeder JI. Abscisic acid and CO₂ signalling via calcium sensitivity priming in guard cells, new CDPK mutant phenotypes and a method for improved resolution of stomatal stimulus–response analyses. Annals of Botany. 2012:**109**(1):5–17. doi:10.1093/aob/mcr252

Hyndman R, Athanasopoulos G, Bergmeir C, Caceres G, Chhay L, O'Hara-Wild M, Petropoulos F, Razbash S, Wang E, Yasmeen F. Forecast: Forecasting functions for time series and linear models. Software, R package. 2022

Hyndman RJ, Khandakar Y. Automatic Time Series Forecasting: the forecast Package for R. Journal of Statistical Software. 2008:**27**(3):1–22. doi:10.18637/jss.v027.i03

Keinath NF, Waadt R, Brugman R, Schroeder JI, Grossmann G, Schumacher K, Krebs M. Live cell imaging with R-GECO1 sheds light on flg22- and Chitin-Induced transient [Ca²⁺]cyt patterns in Arabidopsis. Molecular plant. 2015:**8**(8):1188–1200. doi:10.1016/j.molp.2015.05.006

Kirchner TW, Niehaus M, Debener T, Schenk MK, Herde M. Efficient generation of mutations mediated by CRISPR/Cas9 in the hairy root transformation system of *Brassica carinata*. PLoS One. 2017:**12**(9):e0185429. doi:10.1371/journal.pone.0185429

Klüsener B, Young JJ, Murata Y, Allen GJ, Mori IC, Hugouvieux V, Schroeder JI. Convergence of calcium signaling pathways of pathogenic elicitors and abscisic acid in Arabidopsis guard cells. Plant Physiol. 2002:**130**(4):2152–2163. doi:10.1104/pp.012187

Knorrscheidt A, Püllmann P, Schell E, Homann D, Freier E, Weissenborn MJ. Identification of novel unspecific peroxygenase chimeras and unusual YfeX axial heme ligand by a versatile high-throughput GC-MS approach. ChemCatChem. 2020:**12**(19):4788–4795. doi:10.1002/cctc.202000618

Konrad KR, Wudick MM, Feijó JA. Calcium regulation of tip growth: new genes for old mechanisms. Current Opinion in Plant Biology. 2011:**14**(6):721–730. doi:10.1016/j.pbi.2011.09.005

Köster P, DeFalco TA, Zipfel C. Ca²⁺ signals in plant immunity. The EMBO Journal. 2022:**41**(12):e110741. doi:10.15252/embj.2022110741

Kudla J, Becker D, Grill E, Hedrich R, Hippler M, Kummer U, Parniske M, Romeis T, Schumacher K. Advances and current challenges in calcium signaling. New Phytol. 2018:**218**(2):414–431. doi:10.1111/nph.14966

Kuner T, Augustine GJ. A genetically encoded ratiometric indicator for chloride: capturing chloride transients in cultured hippocampal neurons. Neuron. 2000:**3**(3):447–459. doi:10.1016/S0896-6273(00)00056-8

Li K, Prada J, Damineli DSC, Liese A, Romeis T, Dandekar T, Feijó JA, Hedrich R, Konrad KR. An optimized genetically encoded dual reporter for simultaneous ratio imaging of Ca^{2+} and H^+ reveals new insights into ion signaling in plants. The New Phytologist. 2021:**230**(6):2292–2310. doi:10.1111/nph.17202

Liese A, Romeis T. Biochemical regulation of *in vivo* function of plant calcium-dependent protein kinases (CDPK). Biochimica et Biophysica Acta. 2013:**1833**(7):1582–1589. doi:10.1016/j.bbamcr.2012.10.024

Liu KH, Niu Y, Konishi M, Wu Y, Du H, Sun Chung H, Li L, Boudsocq M, McCormack M, Maekawa S, et al. Discovery of nitrate-CPK-NLP signalling in central nutrient-growth networks. Nature. 2017:**545**(7654):311–316. doi:10.1038/nature22077

Ma SY, Wu WH. AtCPK23 functions in Arabidopsis responses to drought and salt stresses. Plant molecular Biology. 2007:**65**(4):511–518. doi:10.1007/s11103-007-9187-2

Matschi S, Werner S, Schulze WX, Legen J, Hilger HH, Romeis T. Function of calcium-dependent protein kinase CPK28 of *Arabidopsis thaliana* in plant stem elongation and vascular development. The Plant Journal: for Cell and Molecular Biology. 2013:**73**(6):883–896. doi:10.1111/tpj.12090

McClendon CL, Kornev AP, Gilson MK, Taylor SS. Dynamic architecture of a protein kinase. Proceedings of the National Academy of Sciences of the United States of America. 2014:**111**:E4623-4631. doi:10.1073/pnas.1418402111

Menz J, Li Z, Schulze WX, Ludewig U. Early nitrogen-deprivation responses in Arabidopsis roots reveal distinct differences on transcriptome and (phospho-) proteome levels between nitrate and ammonium nutrition. The Plant Journal: for Cell and Molecular Biology. 2016:**88**(5):717–734. doi:10.1111/tpj.13272

Michard E, Dias P, Feijó JA. Tobacco pollen tubes as cellular models for ion dynamics: improved spatial and temporal resolution of extracellular flux and free cytosolic concentration of calcium and protons using pHluorin and YC3.1 CaMeleon. Sex Plant Reprod. 2008:**21**(3):169–181. doi:10.1007/s00497-008-0076-x

Michard E, Simon AA, Tavares B, Wudick MM, Feijó JA. Signaling with ions: The keystone for apical cell growth and morphogenesis in pollen tubes. Plant Physiology. 2017:**173**(1):91–111. doi:10.1104/pp.16.01561

Miyawaki A, Llopis J, Heim R, McCaffery JM, Adams JA, Ikura M, Tsien RY. Fluorescent indicators for Ca^{2+} based on green fluorescent proteins and calmodulin. Nature. 1997:**388**(6645):882–887. doi:10.1038/42264

Monaghan J, Matschi S, Shorinola O, Rovenich H, Matei A, Segonzac C, Malinovsky FG, Rathjen JP, MacLean D, Romeis T, et al. The calcium-dependent protein kinase CPK28 buffers plant immunity and regulates BIK1 turnover. Cell Host & Microbe. 2014:**16**(5):605–615. doi:10.1016/j.chom.2014.10.007

Motulsky HJ, Christopoulos A. Fitting models to biological data using linear and nonlinear regression: A practical guide to curve fitting. Oxford: University Press; 2004.

Mou W, Kao YT, Michard E, Simon AA, Li D, Wudick MM, Lizzio MA, Feijó JA, Chang C. Ethylene-independent signaling by the ethylene precursor ACC in Arabidopsis ovular pollen tube attraction. Nature communications. 2020:**11**(1):4082. doi:10.1038/s41467-020-17819-9

Nagai T, Yamada S, Tominaga T, Ichikawa M, Miyawaki A. Expanded dynamic range of fluorescent indicators for Ca^{2+} by circularly permuted yellow fluorescent proteins. Proceedings of the National Academy of Sciences of the United States of America. 2004:**101**(29):10554–10559. doi:10.1073/pnas.0400417101

Ojo KK, Larson ET, Keyloun KR, Castaneda LJ, DeRocher AE, Inampudi KK, Kim JE, Arakaki TL, Murphy RC, Zhang L, et al. *Toxoplasma gondii* calcium-dependent protein kinase 1 is a target

for selective kinase inhibitors. Nature structural & Molecular Biology. 2010:**17**(5):602–607. doi:10.1038/nsmb.1818

Ooms, J. Zero-dependency data frame to xlsx exporter based on 'libxlsxwriter'. Fast and no Java or Excel required. 2021

Patton C, Thompson S, Epel D. Some precautions in using chelators to buffer metals in biological solutions. Cell calcium. 2004:**35**(5):427–431. doi:10.1016/j.ceca.2003.10.006

Rappsilber J, Ishihama Y, Mann M. Stop and go extraction tips for matrix-assisted laser desorption/ionization, nanoelectrospray, and LC/MS sample pretreatment in proteomics. Analytical chemistry. 2003:**75**(3):663–670. doi:10.1021/ac026117i

R Core Team. R: A language and environment for statistical computing 1. https://www.R-project.org. 2022

Saris NE, Mervaala E, Karppanen H, Khawaja JA, Lewenstam A. Magnesium. An update on physiological, clinical and analytical aspects. Clinica chimica acta; international journal of clinical chemistry. 2000:**294**(1-2):1–26. doi:10.1016/S0009-8981(99)00258-2

Scherzer S, Maierhofer T, Al-Rasheid KAS, Geiger D, Hedrich R. Multiple calcium-dependent kinases modulate ABA-activated guard cell anion channels. Molecular Plant. 2012:**5**(6):1409–1412. doi:10.1093/mp/sss084

Schindelin J, Arganda-Carreras I, Frise E, Kaynig V, Longair M, Pietzsch T, Preibisch S, Rueden C, Saalfeld S, Schmid B, et al. Fiji: an open-source platform for biological-image analysis. Nature methods. 2012:**9**(7):676–682. doi:10.1038/nmeth.2019

Schlücking K, Edel KH, Köster P, Drerup MM, Eckert C, Steinhorst L, Waadt R, Batistič O, Kudla J. A new β-estradiol-inducible vector set that facilitates easy construction and efficient expression of transgenes reveals CBL3-dependent cytoplasm to tonoplast translocation of CIPK5. Molecular Plant. 2013:**6**(6):1814–1829. doi:10.1093/mp/sst065

Schmidt A, Beck M, Malmström J, Lam H, Claassen M, Campbell D, Aebersold R. Absolute quantification of microbial proteomes at different states by directed mass spectrometry. Molecular Systems Biology. 2011:**7**(1):510. doi:10.1038/msb.2011.37

Schmidt TG, Skerra A. The Strep-tag system for one-step purification and high-affinity detection or capturing of proteins. Nature Protocols. 2007:**2**(6):1528–1535. doi:10.1038/nprot.2007.209

Schneider TD, Stephens RM. Sequence logos: a new way to display consensus sequences. Nucleic acids Research. 1990:**18**(20):6097–6100. doi:10.1093/nar/18.20.6097

Schroeder MJ, Shabanowitz J, Schwartz JC, Hunt DF, Coon JJ. A neutral loss activation method for improved phosphopeptide sequence analysis by quadrupole ion trap mass spectrometry. Analytical chemistry. 2004:**76**(13):3590–3598. doi:10.1021/ac0497104

Simeunovic A, Mair A, Wurzinger B, Teige M. Know where your clients are: subcellular localization and targets of calcium-dependent protein kinases. Journal of Experimental Botany. 2016:**67**(13):3855–3872. doi:10.1093/jxb/erw157

Sudarshana MR, Plesha MA, Uratsu SL, Falk BW, Dandekar AM, Huang TK, McDonald KA. A chemically inducible cucumber mosaic virus amplicon system for expression of heterologous proteins in plant tissues. Plant Biotechnology Journal. 2006:**4**(5):551–559. doi:10.1111/j.1467-7652.2006.00202.x

Tan YQ, Yang Y, Shen X, Zhu M, Shen J, Zhang W, Hu H, Wang YF. Multiple cyclic nucleotide-gated channels function as ABA-activated Ca^{2+} channels required for ABA-induced stomatal closure in Arabidopsis. The Plant cell. 2022:**35**(1):239–259. doi:10.1093/plcell/koac274

Team R. RStudio: Integrated Development Environment for R. RStudio. PBC, Boston. MA. 1. 2022

Thor K, Jiang S, Michard E, George J, Scherzer S, Huang S, Dindas J, Derbyshire P, Leitão N, DeFalco TA, et al. The calcium-permeable channel OSCA1.3 regulates plant stomatal immunity. Nature. 2020:**585**(7826):569–573. doi:10.1038/s41586-020-2702-1

Thor K, Peiter E. Cytosolic calcium signals elicited by the pathogen-associated molecular pattern flg22 in stomatal guard cells are of an

oscillatory nature. The New Phytologist. 2014:**204**(4):873–881. doi:10.1111/nph.13064

Tian W, Hou C, Ren Z, Wang C, Zhao F, Dahlbeck D, Hu S, Zhang L, Niu Q, Li L, et al. A calmodulin-gated calcium channel links pathogen patterns to plant immunity. Nature. 2019:**572**(7767):131–135. doi:10.1038/s41586-019-1413-y

Tian W, Wang C, Gao Q, Li L, Luan S. Calcium spikes, waves and oscillations in plant development and biotic interactions. Nature Plants. 2020:**6**(7):750–759. doi:10.1038/s41477-020-0667-6

Toyota M, Spencer D, Sawai-Toyota S, Jiaqi W, Zhang T, Koo AJ, Howe GA, Gilroy S. Glutamate triggers long-distance, calcium-based plant defense signaling. Science. 2018:**361**(6407):1112–1115. doi:10.1126/science.aat7744

UniProt Consortium. UniProt: the universal protein knowledgebase in 2021. Nucleic Acids Research. 2021:**49**(D1):D480–D489. doi:10.1093/nar/gkaa1100

Waadt R, Hitomi K, Nishimura N, Hitomi C, Adams SR, Getzoff ED, Schroeder JI. FRET-based reporters for the direct visualization of abscisic acid concentration changes and distribution in Arabidopsis. eLife. 2014:**3**:e01739. doi:10.7554/eLife.01739

Waadt R, Köster P, Andrés Z, Waadt C, Bradamante G, Lampou K, Kudla J, Schumacher K. Dual-reporting transcriptionally linked genetically encoded fluorescent indicators resolve the spatiotemporal coordination of cytosolic abscisic acid and second messenger dynamics in Arabidopsis. The Plant cell. 2020:**32**(8):2582–2601. doi:10.1105/tpc.19.00892

Waadt R, Krebs M, Kudla J, Schumacher K. Multiparameter imaging of calcium and abscisic acid and high-resolution quantitative calcium measurements using R-GECO1-mTurquoise in Arabidopsis. The New Phytologist. 2017:**216**(1):303–320. doi:10.1111/nph.14706

Wang Z, Gou X. The first line of defense: Receptor-like protein kinase-mediated stomatal immunity. International Journal of Molecular Sciences. 2021:**23**(1):343. doi:10.3390/ijms23010343

Weber E, Engler C, Gruetzner R, Werner S, Marillonnet S. A modular cloning system for standardized assembly of multigene constructs. PLoS One. 2011:**6**(2):e16765. doi:10.1371/journal.pone.0016765

Weiner MP, Costa GL, Schoettlin W, Cline J, Mathur E, Bauer JC. Site-directed mutagenesis of double-stranded DNA by the polymerase chain reaction. Gene. 1994:**151**(1-2):119–123. doi:10.1016/0378-1119(94)90641-6

Wernimont AK, Amani M, Qiu W, Pizarro JC, Artz JD, Lin YH, Lew J, Hutchinson A, Hui R. Structures of parasitic CDPK domains point to a common mechanism of activation. Proteins. 2011:**79**(3):803–820. doi:10.1002/prot.22919

Wernimont AK, Artz JD, Finerty P, Lin YH, Amani M, Allali-Hassani A, Senisterra G, Vedadi M, Tempel W, Mackenzie F, et al. Structures of apicomplexan calcium-dependent protein kinases reveal mechanism of activation by calcium. Nature Structural & Molecular Biology. 2010:**17**(5):596–601. doi:10.1038/nsmb.1795

Wickham H, Seidel D, R Studio. Graphical scales map data to aesthetics, and provide methods for automatically determining breaks and labels for axes and legends. 2022a.

Wickham H, Bryan J, R Studio. readxl: Read Excel Files. 2022b.

Winter D, Vinegar B, Nahal H, Ammar R, Wilson GV, Provart NJ. An "Electronic Fluorescent Pictograph" browser for exploring and analyzing large-scale biological data sets. PLoS One. 2007:**2**(8):e718. doi:10.1371/journal.pone.0000718

Witte CP, Noël L, Gielbert J, Parker J, Romeis T. Rapid one-step protein purification from plant material using the eight-amino acid StrepII epitope. Plant Molecular Biology. 2004:**55**(1):135–147. doi:10.1007/s11103-004-0501-y

Wu F-H, Shen S-C, Lee L-Y, Lee S-H, Chan M-T, Lin C-S. Tape-arabidopsis sandwich—a simpler arabidopsis protoplast isolation method. Plant Methods. 2009:**5**(1):16. doi:10.1186/1746-4811-5-16

Xu G, Moeder W, Yoshioka K, Shan L. A tale of many families: calcium channels in plant immunity. The Plant cell. 2022:**34**(5):1551–1567. doi:10.1093/plcell/koac033

Yip Delormel T, Boudsocq M. Properties and functions of calcium-dependent protein kinases and their relatives in *Arabidopsis thaliana*. The New Phytologist. 2019:**224**(2):585–604. doi:10.1111/nph.16088

Yuan F, Yang H, Xue Y, Kong D, Ye R, Li C, Zhang J, Theprungsirikul L, Shrift T, Krichilsky B, et al. OSCA1 mediates osmotic-stress-evoked Ca²⁺ increases vital for osmosensing in Arabidopsis. Nature. 2014:**514**(7522):367–371. doi:10.1038/nature13593

Zaman N, Seitz K, Kabir M, George-Schreder LS, Shepstone I, Liu Y, Zhang S, Krysan PJ. A Förster resonance energy transfer sensor for live-cell imaging of mitogen-activated protein kinase activity in Arabidopsis. The Plant Journal: for Cell and Molecular Biology. 2019:**97**(5):970–983. doi:10.1111/tpj.14164

Zhang L, Takahashi Y, Hsu PK, Kollist H, Merilo E, Krysan PJ, Schroeder JI. FRET kinase sensor development reveals SnRK2/OST1 activation by ABA but not by MeJA and high CO₂ during stomatal closure. eLife. 2020:**9**. doi:10.7554/eLife.56351

Zhao Y, Araki S, Wu J, Teramoto T, Chang YF, Nakano M, Abdelfattah AS, Fujiwara M, Ishihara T, Nagai T, et al. An expanded palette of genetically encoded Ca²⁺ indicators. Science. 2011:**333**(6051):1888–1891. doi:10.1126/science.1208592

Zhou JY, Hao DL, Yang GZ. Regulation of cytosolic pH: The contributions of plant plasma membrane H⁺-ATPases and multiple transporters. International Journal of Molecular Sciences. 2021:**22**(23):12998. doi:10.3390/ijms222312998

Zimmermann T, Rietdorf J, Girod A, Georget V, Pepperkok R. Spectral imaging and linear un-mixing enables improved FRET efficiency with a novel GFP2-YFP FRET pair. FEBS letters. 2002:**531**(2):245–249. doi:10.1016/S0014-5793(02)03508-1

Zuo J, Niu QW, Chua NH. Technical advance: An estrogen receptor-based transactivator XVE mediates highly inducible gene expression in transgenic plants. The Plant Journal: for Cell and Molecular Biology. 2000:**24**(2):265–273. doi:10.1046/j.1365-313x.2000.00868.x